Density Functional Studies on the Lone Pair Effect of the Trivalent Group (V) Elements: I. Electronic Structure, Vibronic Coupling, and Chemical Criteria for the Occurrence of Lone Pair Distortions in AX_3 Molecules (A=N to Bi; X=H, and F to I)

M. Atanasov[†,‡] **and D. Reinen***[,†]

Fachbereich Chemie der Philipps-Universität und Zentrum für Materialwissenschaften, Hans-Meerweinstr.1, D-35043 Marburg, Germany, and Institute of General and Inorganic Chemistry, Bulgarian Academy of Sciences, Bl.11 Sofia 1113, Bulgaria

Received: December 15, 2000; In Final Form: March 9, 2001

The energetic, steric, and bonding properties of molecules AX_3 (A=N to Bi; X=H, F to I) are analyzed using density functional theory. It is found that the "lone pair" in the initial D_{3h} geometry is of central atom p_z character for the NX_3 and AH_3 molecules, whereas it possesses *s* symmetry in all other cases − here generally with a strong delocalization toward the ligands. The stabilization of the distorted C_{3v} geometry is due mainly to covalency effects, whereas steric interaction forces according to the Gillespie−Nyholm model do not seem to play a significant role. The application of the conventional vibronic pseudo Jahn−Teller coupling approach (PJT), here for the $D_{3h}\rightarrow C_{3v}$ transition $[A_1'\otimes(\alpha_2'' + \alpha_1')\otimes A_2'']$ interaction], is an appropriate means for inorganic chemists to predict trends for the extent of distortion and for the corresponding energy gain. The vibronic coupling constants and the vibronic stabilization energies, which mainly determine the total $D_{3h}\rightarrow C_{3v}$ energy gain, vary according to the sequences F > H > Cl > Br > I (A: N to Bi), and N > P > As > Sb > Bi (X: H,F), the dependence on A being only small or not present (X: Cl to I). Thus, the hardest molecules are the most susceptible to vibronic coupling, the latter energy being approximately imaged by the hardness difference $\eta(C_{3v}) - \eta(D_{3h})$. A roughly inverse trend is observed if the extent of the angular distortion τ_α from D_{3h} to C_{3v} symmetry is considered; here, the softest molecules such as $Sb(Bi)Br_3$ exhibit the largest and NH_3 the smallest deviations from D_{3h} geometry. The different sequences for τ_α are due to the strong influence of the force constant, which represents the $C_{3v}\rightarrow D_{3h}$ restoring energy. It is remarkable that the vibronic coupling energy is strongly correlated with the chemical hardness η (an observable quantity), while the stabilization energy for the $D_{3h}\rightarrow C_{3v}$ transition is not directly reflected by η, in contrast to what is generally called the "principle of maximum hardness".

I. Introduction

In this study we explore by means of density functional theory (DFT) the stereochemical activity of a single lone pair in the title series compounds and use these results to critically evaluate the predictive power of the two models describing such activities, the valence shell electron pair repulsion (VSEPR) and the vibronic pseudo Jahn−Teller (PJT) coupling models.

The cations of the third to seventh main group occur not only in the highest possible oxidation states but also in oxidation states that are lower by 2 [for example In(III,I), Tl(III,I); Sn(IV,II), Pb(IV,II); Sb(V,III),Bi(V,III); etc.]. In a chemical environment, the latter possess an ns^2 (or in certain cases, see below, an np^2) configuration ($n = 2-6$), which may lead to electronic and stereochemical instability if np (ns) orbital contributions are admixed, rendering directional properties to the "lone pair". It has been proposed[1−3] that the electrostatically most favorable distribution of all electron pairs in the valence shell of a central atom dictates the molecular geometry (VSEPR model). In many cases, however, solely the repulsive forces between the ligator atoms seem to govern the geometry, the lone pairs being "inert", i.e. included in the spherically symmetric core.[4] The pioneering work by Bader et al.,[5] based on a topological analysis of the Laplacian of the electron density, gives a physical basis for the VSEPR model of molecular geometry. Despite the availability of widespread structural and spectroscopic results and theoretical[6] studies, it is not clear up to now, however, whether the forces leading to molecular distortions (lone pair effect) are dominated by repulsive interactions between valence and lone pair electron pairs, demanded by the VSEPR model, or by the energy gain due to orbital overlap effects as one distorts nuclear configurations from higher to lower symmetry. We focus on systems with the coordination number (CN) equal to 3 such as Bi^{III} and the other trivalent elements of the fifth main group, including relativistic corrections into the calculations. The results are generally compared with those for the analogous polyhedra of Tl^{III}. The latter cation possesses the same formal charge as Bi^{III} and an electronic configuration corresponding to that of Bi^{III} without the lone pair, hence lacking a possible stereochemical activity. We in particular analyze how the extent of the stereochemical effect and the extent of the energetic stabilization vary, if the central ion changes from N^{III} via P^{III}, As^{III}, Sb^{III} to Bi^{III} and the ligand from F^- to I^-, and finally to hydride. In a second contribution we

---

* Corresponding author. Fax: (+49) 6421 2828917. E-mail: reinen@ps1515.chemie.uni-marburg.de

[†] Fachbereich Chemie der Philipps-Universität und Zentrum für Materialwissenschaften.

[‡] Institute of General and Inorganic Chemistry.

10.1021/jp004511j CCC: \$20.00

will extend our investigation to complexes of lower and higher coordination numbers. In contrast to the model case of CN = 3, these are positively (CN = 2) or negatively (CN = 4−6) charged, however. Here DFT provides the possibility to compensate the charge by introducing a polarizable solvent environment, thus stabilizing the ionic species.

The purpose of this study is twofold. On one hand, we intend to derive simple rules, which allow the chemist to predict whether compounds will show a steric lone pair effect or not and how large the distortion might be. On the other hand, we want to demonstrate the significance of the vibronic coupling model for the understanding of the energetic and stereochemical stabilization of this kind of molecules and solids. Such concept bears reality, because vibronic interactions connected with lone pair cations such as Bi^{III} are considered to give rise to other interesting phenomena in materials science; thus, the mixed valence oxide ceramics $Bi_{0.6}K_{0.4}BiO_{2.93}$ and $BaBi_{0.25}Pb_{0.75}O_3$, for example, exhibit superconducting properties with critical temperatures of ≈30 K and ≈16 K, respectively.[7] In future studies we want to extend our investigations to solids, where cooperative elastic and electronic interactions between neighbored cationic centers and host lattice strains add to the local lone pair effect, yielding rather complex situations in many cases.

Predictions of the Gillespie−Nyholm Model. The geometrical patterns due to lone pair activity are predicted and interpreted within the VSEPR model developed by Sidgwick and Powell,[1] Gillespie and Nyholm,[2] and others.[3−5] This model assumes that (i) the valence charge density is spatially localized into pairs of electrons and (ii) the geometrical arrangement of the ligands is that which maximizes the interpair separation and minimizes the interpair repulsion, including both bonded and lone pairs. The shape of the polyhedra predicted on this basis for cations with a single lone pair is of C_{3v} (trigonal pyramid) symmetry for the CN = 3, with the trigonal-planar (D_{3h}) coordination as the parent geometry of the highest possible symmetry. While the predictions of the VSEPR model for the CNs 2 to 5 are unambiguous, they become less definite for the CN = 6 and higher CNs. Electrostatic arguments suggest polyhedra with C_{2v} and C_{3v} symmetry for the CN = 6, which correspond to a pentagonal bipyramid with one missing ligand in the equatorial plane and a monocapped octahedron, the lone pair occupying the cap position, respectively. The experimental finding is different, however. Either undistorted octahedra occur, implying a spherical ns^2 pair or a dynamic averaging of equivalent distorted conformations,[8] or a tetragonal pyramid (C_{4v})[9a] is observed, resulting from the removal of one ligand along a 4-fold axis of the octahedron. While the Gillespie−Nyholm rules would derive the latter geometry from the CN = 5, a trigonal-bipyramid (D_{3h}), there is experimental evidence that the parent symmetry can be O_h-(CN = 6) as well. We will discuss these items in a subsequent paper.

Predictions by the Vibronic Coupling Model. One can alternatively look at coordinated lone pair cations starting from the highest possible geometry for the considered coordination number, say D_{3h} (CN = 3), and consider lower-symmetry distortions along certain normal mode distortion coordinates with the property that the $ns^2(^1A_1')$ ground state and a neighbored ns^1p^1 $(^1A_2'')$ excited state adopt the same symmetry and hence may interact (pseudo Jahn−Teller effect, PJTE,[10,11]). Group theory allows to select the vibronically active vibration υ by inspecting the direct product $^1A_1'\otimes\upsilon\otimes{}^1A_2''$, which has to contain the totally symmetric representation. The active mode is α_2'' in this case, leading from the D_{3h} into the distorted C_{3v} molecular geometry:

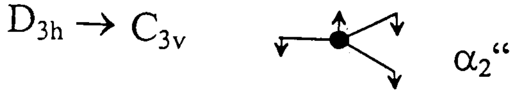

We want to emphasize at this stage that the vibronic model does not introduce novel interactions between the atomic fragments but merely represents a different kind of parametrization, which is more illustrative and comprehensive than conventional concepts such as the electrostatic VSEPR model, for example. The vibronic coupling effect can be looked at as creating a "new covalency,"[11b] in addition to some smaller ionic (crystal field) interactions, in the course of distortion. We will discuss this matter in greater detail when we compare the various energy parameters resulting from the vibronic approach, with the electrostatic and covalency bond contributions, which emerge from the DFT calculations for the $D_{3h}\leftrightarrow C_{3v}$ interconversion (see eq 9).

The PJT concept is imaged by the coupling matrix of eq 1, the critical parameters being the $^1A_2''(ns^1p^1)-{}^1A_1'(ns^2 \text{ or } np_z^2$, see below) separation Δ and the nondiagonal vibronic coupling constant t_α, which parametrizes the s−p mixing due to distortions along the vibronically active α_2'' mode (τ_α).

$$\begin{array}{cc} {}^1A_1' & {}^1A_2'' \\ \left[\begin{array}{c} E_g - E \\ t_\alpha\tau_\alpha \end{array}\right. & \left.\begin{array}{c} t_\alpha\tau_\alpha \\ E_e - E \end{array}\right] \end{array} \tag{1}$$

where $t_\alpha = \langle\Psi(A_1')|\delta H/\delta\tau_\alpha\,|\Psi(A_2'')\rangle$, $E_g = (1/2)K_\alpha\tau_\alpha^2$, and $E_e = (1/2)K_\alpha'\tau_\alpha^2 + \Delta$. E_g and E_a contain the restoring force energies for the ground and the excited state respectively, which favor the higher symmetry. Equation 2 gives solutions of the matrix (eq 1); here E_+ and E_- refer to the $A_1(^1A_2'')$ and $A_1(^1A_1')$ states in C_{3v}, after the vibronic interaction:

$$E_\pm=(1/2)\{E_g + E_e \pm [\delta E_{g,e}{}^2 + 4\,(t_\alpha\tau_\alpha)^2]^{1/2}\},$$
$$\text{with } \delta E_{g,e} = \Delta + (1/2)(K_\alpha' - K_\alpha)\tau_\alpha^2 \tag{2}$$

$$t_\alpha = 0 \qquad E_- = (1/2)K_\alpha\tau_\alpha^2 \tag{2a}$$

$$(t_\alpha\tau_\alpha)^2 \ll \delta E_{g,e}{}^2/4 \qquad E_- \cong (1/2)[K_\alpha - 2t_\alpha^2/\delta E_{g,e}]\tau_\alpha^2 \tag{2b}$$

$$t_\alpha\tau_\alpha \gg \delta E_{g,e}/2 \qquad E_- \approx (1/2)K_\alpha\tau_\alpha^2 - t_\alpha\tau_\alpha \tag{2c}$$

Figure 1 illustrates the three possible limiting approximations for the strength of the PJT coupling by schematic potential curve diagrams. Figure 1a refers to vanishing vibronic interaction (eq 2a), such as is the case for Tl^{III}, and Figure 1b characterizes the weak coupling case, leading to a flattening of the E_- potential curve (soft-mode behavior along τ_α) by ns-np$_z$ mixing (eq 2b) with an effective force constant $K_\alpha^{eff} = K_\alpha - 2t_\alpha^2/\delta E_{g,e}$. Only in the strong coupling case of Figure 1c, eq 2c, a new minimum ($E_-<0$) at a finite value of the nuclear displacement parameter τ_α develops. The minimum position and the energy gain E_-^m in the latter case is given in eq 3.

$$(t_\alpha\tau_\alpha)^2 \gg \delta E_{g,e}{}^2/4 \quad \tau_\alpha^m \cong t_\alpha/K_\alpha \tag{3}$$

$$t_\alpha\tau_\alpha \gg \delta E_{g,e}/2 \qquad E_-^m \approx -(1/2)t_\alpha\tau_\alpha^m \Rightarrow t_\alpha \approx -2E_-^m/\tau_\alpha^m$$

The given expressions readily allow to calculate the vibronic

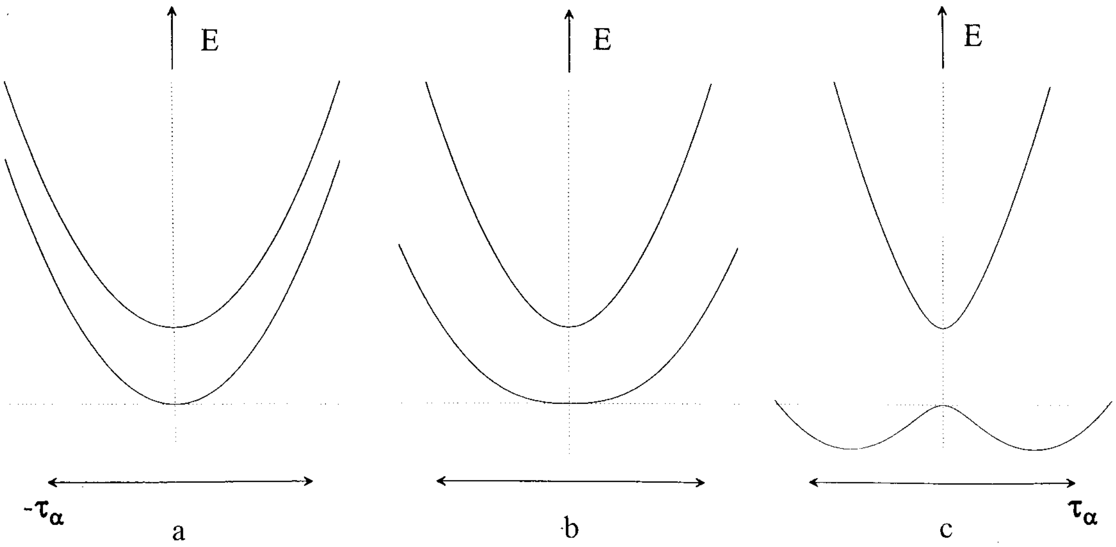

Figure 1. Potential curves of the interacting ground ($6s^2$ or $6p_z^2$) and excited ($6s^1p_z^1$) states of, for example, octahedrally coordinated Bi^{III} by vibronic PJT interaction along the $\alpha_2''(\tau_\alpha)$ distortion coordinate (schematic). They illustrate the cases of vanishing [a; eq 2a], weak [b; eq 2b], and strong coupling [c; eq 2c].

coupling parameter t_α from energy values and geometric parameters available from experiment and the DFT calculations (see below). Even in the strong coupling case, a system may retain the higher parent symmetry [dynamic averaging between the two equivalent C_{3v} nuclear displacements ($+\tau_\alpha$) and ($-\tau_\alpha$)]. Usually, however, symmetry breaking due to external forces, such as encountered as strains in crystals, occurs and leads to a static distortion.

We should note here that matrix (1), and its more sophisticated form (5a) as well, is restricted to linear vibronic coupling terms and a two-level system (see section IV.1 and below). As such it is valid, in a strict sense, only for small nuclear displacements from the reference geometry, leading (by perturbational expansion up to second-order energy terms) to the approximate solution (eq 2b); this kind of treatment became a common procedure in the vibronic theory of stereochemistry (see the overview in ref 11b). Our analysis, however, is based on *exact* solutions of matrices (1) and (5), allowing to consider also larger distortions from the parent geometry when assuming that the linear coupling term dominates the higher order terms.

As has been demonstrated by the analysis of a large number of structural and spectroscopic data,[4] the more sophisticated symmetry concept of the PJTE model is superior to that of the straightforwardly applicable VSEPR model, though admittedly more complex. Whereas the concept of the PJTE predicts the symmetry aspects of the lone pair effect correctly in most cases, the model does not specify the alterations of the bond properties during the symmetry change, which are energetically in its essential part represented by the vibronically interacting HOMO and LUMO (see section III). However, the MO schemes derived from DFT allow to analyze the central ion and ligand contributions in the respective molecular orbitals (MOs) and also give detailed information as to whether the energy gain by the transition from the "symmetric" to the "distorted" geometry is caused exclusively by the stabilization of the "lone pair" HOMO and lower-lying MOs of the same symmetry or if other MOs are involved as well. A correct vibronic interaction treatment should take into account the presence of further excited A_2'' states, which may couple with the A_1' ground state as well. Though the separation energy Δ is rather large in such cases, the coupling constants t_α may also be considerably larger and produce additional distinct energetic stabilization effects. This point will be considered in section IV and the appendix.

In this and the following contribution we intend to simulate the stereochemical lone pair effect by DFT calculations, in order to gain some insight about the accompanying energy changes. Our main intention is to obtain information about the dependence of the geometrical and electronic instability on the nature of the ligand, the position of the central ion in the periodic table, and the coordination number of the considered polyhedra. The authors are aware that the calculational results have to be considered with precaution, avoiding an overinterpretation with respect to the quantitative relevance. Nevertheless, the fast availability of data makes DFT a valuable tool for the chemist to get a deeper-going understanding of the lone pair phenomenon − quod est demonstrandum.

II. Computational Details

Spin-restricted DFT calculations have been carried out with the Amsterdam density functional (ADF) program package (versions ADF.2.3 and, recently ADF1999).[12−15] The Vosko−Wilk−Nusair parametrization[16] of the electron gas data has been used for the exchange correlation energy and potential. Density gradient corrections were included for the exchange[17] and for the correlation.[18] To check the reliability of the basis sets for Bi and Tl supplied by the ADF 2.3 and ADF1999 packages and their effect on the Kohn−Sham orbital energies, we have performed calculations on the BiF_3 cluster using basis sets with improved quality from double-ζ to triple-ζ and accounting for relativistic effects (scalar and spin−orbit coupling) and inner shell orbitals ($4f^{14}5s^2p^6d^{10}$); subsequently the optimized geometries and bond energy changes during the $D_{3h}\rightarrow C_{3v}$ transition were compared with results from MP2 calculations.[6] Best agreement between calculated geometrical parameters and energies for BiF_3 and literature data is achieved using triple-ζ Slater type orbitals (STOs) extended by one polarization function (TZP) for Bi, F, and O and frozen core 1s orbitals of F and O. In calculating the energies, separate *atomic* fragments have been chosen as the reference, if not stated otherwise. Relativistic effects were included using a perturbative quasirelativistic (Pauli) Hamiltonian and, alternatively, a variational zero order regular approximation (ZORA), with and without spin−orbit coupling.

DFT orbitals and their energies have been calculated by solving the Kohn−Sham equations, where both electronic exchange and correlation were taken into account. As such, these orbitals are superior to those calculated using Hartree−Fock theory, in which electronic exchange (Fermi hole) is accounted for accurately, but electronic correlation (the correlation hole) is completely neglected. As has been recently shown, Kohn−Sham orbitals are chemically significant[19] and can be used as valuable substitute for MOs resulting from extended Hückel calculations.[20] Kohn−Sham equations and Kohn−Sham orbitals, which we will simply call MOs in the following, are very useful in the sense that they image the total energy and its components, such as Coulomb attractive and repulsive forces, projected onto single orbital configurations.

The total bonding energies (E_t) have been analyzed using the transition state method of Ziegler and Rauk.[21] In this method E_t is decomposed into three terms. The first term is the electrostatic energy, calculated for the *unrelaxed* densities of the atomic fragments (E_{el}). It consists of repulsive terms due to nuclear−nuclear and electron−electron interactions, as well as attractive interactions between the electrons on a given fragment and the nuclei of the other fragments. The second contribution stems from the overlap between closed shells of different atoms, again for the unrelaxed situation. This gives rise to a Pauli exchange repulsive term (E_P). Finally, the change in electronic density of the starting atomic fragments due to charge transfer (CT) between singly or doubly occupied to singly occupied and empty orbitals is considered. This is a bonding contribution and is referred to as the orbital interaction energy (E_{orb}). The three energy contributions to E_t and E_t itself are of different magnitudes, if not the atomic components of the respective compound or polyhedron but ionic fragments (a possibly more suitable choice for clusters with higher ionicity) are chosen. However, the difference between the bonding energies (δE_t) of the same AX_3 molecule in D_{3h} and C_{3v} is independent of this choice. Because molecules dissociate into neutral atoms, rather than into charged ions, the total bonding energy as obtained using atomic fragments should be used for comparison with the bond dissociation energy.

The sum of E_{el} and E_P, pertaining to the nonrelaxed fragments, is sometimes considered to be the "steric interaction energy" (E_o).[21] However, following the arguments in a recent paper by Diefenbach et al.,[22] we prefer to discuss the three energy components of E_t separately, hereby looking at E_{el} and E_{orb} as representing the major part of the ionic and covalent bond contributions, respectively. We further propose to correlate E_P with the steric interaction underlying the VSEPR model. E_P is large at small interatomic distances and hence expected to dominate the electron pair repulsion energy. Though electrostatic (Coulomb) interactions are also involved in the steric interaction, $|E_{el}|$ (at interatomic distances close to the equilibrium ones) is always much smaller than $|E_P|$, at least in the cases considered here, thus supporting to consider E_P as approximately representing the VSEPR energy. While the VSEPR model is a pragmatic concept lacking an exact physical basis, the Pauli repulsion term has the advantage to be a well defined and calculable quantity. We will, referring to the arguments in this discussion, use E_P in the following as the "steric repulsion", which broadly images the VSEPR energy.

We use a Mulliken population analysis (MPA) in order to specify the percentage of a given atomic orbital in the MO and to calculate effective atomic charges. Because in MPA the overlap charge is divided half between the contributing orbitals, in some cases, such as encountered for antibonding MO's, a negative percentage in a given MO may result. It is well-known, that the charges obtained by projecting on local orbitals are notoriously sensitive to the choice of basis functions. Thus, Mulliken charges will be used only in a comparative way.

Furthermore, we have calculated the chemical potential μ and the hardness η, which are important energy quantities, when imaging the total energy. They are deduced from the first and second derivative of the total energy with respect to the number of electrons (N) in the constant potential v of the nuclear subsystem, referred to as an "external" potential [eq 4a].[23,24] However, as has been discussed elsewhere,[24] μ and η are discontinuous functions for systems with a finite HOMO−LUMO separation, but with a much smaller discontinuity gap in the latter case. Explicitely, we have derived μ and η using eq 4b, where the ϵ are Kohn−Sham orbital energies. They are correlated with the total energy change in dependence on the number of electrons (n) in the HOMO or LUMO by $\epsilon = (\partial E_t/\partial n)_v$ and $U = (\partial \epsilon/\partial n)_v$, where U has the meaning of an effective interelectronic repulsion energy, related to the one used in the Hubbard model. The thus defined quantities μ and η approximately equal the (negative) electronegativity χ and the chemical hardness, respectively, generally applied in chemistry and based on the ionization energy (I) and the electron affinity (A) [eq 4c].[24] μ and η are calculated by removing (adding) only fractional electron density (here in steps ±0.05 e) from (to) the system according to eq 4a. They are considered to yield more accurate values than those values based on an integer number of electrons [eq 4c] and not derived from energy values in the close vicinity of the neutral molecule.

$$\mu = (\partial E_t/\partial N)_v \qquad \eta = (1/2)(\partial^2 E_t/\partial N^2)_v \tag{4a}$$

$$\mu = (1/2)[(\epsilon_{LUMO} + \epsilon_{HOMO}) - (U_{HOMO} - U_{LUMO})] \tag{4b}$$

$$\eta = (1/2)[(\epsilon_{LUMO} - \epsilon_{HOMO}) + (U_{HOMO} + U_{LUMO})]$$

$$\mu \approx -\chi = -(I + A)/2 \qquad \eta \approx (I-A)/2 \tag{4c}$$

We mention finally that we have used floating basis functions in the DFT calculations, meaning that the respective electron densities follow the nuclear displacement during the symmetry change. This approach has the advantage with respect to that based on space-fixed atomic orbitals that only the physically meaningful bonding properties, namely the electronic rearrangement and the corresponding change of overlap, are considered, as has been pointed out by Bersuker et al.[25]

III. Results and Discussion

1. BiF_3 and BiH_3. We start to consider bismuth compounds for three reasons. First the stereochemistry of Bi^{III} in oxidic solids is governed by static lone pair distortions,[9] second we were interested in exploring the importance of relativistic corrections for the lone pair effect, and third the lone pair effect might be significant for the superconducting properties of certain Bi^{III} oxide ceramics.[7]

The DFT geometry optimization for BiF_3 shows that the trigonal pyramidal geometry (C_{3v}) is stabilized by $\delta E_t = -1.16$ eV (relativistic calculation) with respect to the planar (D_{3h}) coordination. Geometrical parameters and bonding energy changes are listed in Table 1. The Bi−F bond length decreases by ≅0.06 Å, proceding from the D_{3h} to the C_{3v} coordination, reflecting a strengthening of the Bi−F bonds in the distorted geometry. This observation is in accord with the expectation, because the F^- ligands will be repelled by an electron pair with pure s character, in difference to the repulsive force of a lone

TABLE 1: Calculated Energies [δE_t, δE_P, δE_{el}, δE_{orb} and Its Components from the $a_1(a_1',a_2'')$ and $e(e',e'')$ MOs, δ − $(A_2''-A_1')$ Separation, in eV] and Geometrical Parameters (Bond Lengths *R* in Å and F(H)−A−F(H) Angles α in Degrees with the Experimental Values[a] in Parentheses) for Molecules AF_3 and AH_3 (A^{III}: N,P,As,Sb,Bi) and TlF_3 for Comparing Purposes[b]

	δE_t	δE_P	δE_{el}	δE_{orb}[c]	$\delta E_{orb}(a_1)$	$\delta E_{orb}(e)$	δ	$R(D_{3h})$	$R(C_{3v})$	$\alpha(C_{3v})$	$q(D_{3h})$	$q(C_{3v})$	$\delta E_{a2''}$(%A)	$\delta E_{a1'}$(%A)
NF_3	−3.46	−10.63	2.45	4.73	−5.61	10.25	1.10[d]	1.36	1.40(1.37)	101.9(102.1)	1.10	0.87	−3.9(67)[d]	2.0(42)
	−3.45	−4.87	3.59	−2.18	−1.66	−0.64								
PF_3	−2.72	12.67	−4.08	−11.31	−11.28	−0.02	1.78	1.73	1.63(1.56)	97.3(97.7)	1.43	1.44	5.5(79)	−1.4(40)
	−2.72	6.46	−3.30	−5.88	−5.74	−0.11								
AsF_3	−2.04	9.88	−3.42	−8.51	−8.73	0.25	2.23	1.84	1.75(1.70)	96.5(95.8)	1.69	1.82	4.6(79)	−1.2(30)
	−1.96	5.16	−2.85	−4.27	−4.04	−0.19								
SbF_3	−1.66	6.58	−2.40	−5.84	−6.61	0.81	2.46	2.02	1.94(1.88)	95.8(95.0)	1.72	1.86	3.8(83)	−1.1(34)
	−1.67	3.61	−1.77	−3.51	−3.40	−0.08								
BiF_3	−1.16	4.85	−1.81	−4.20	−5.50	1.32	3.03	2.10	2.04(1.98)	94.3(96.5)	1.77	1.84	3.2(84)	−0.8(19)
	[−1.02]	[−0.02]	[−0.02]	[−0.98]	[−4.28]	[3.24]								
	−1.16	2.79	−0.90	−3.05	−2.79	−0.24								
TlF_3								2.03		120	1.66		(96)	(67)
NH_3	−0.23	−2.97	−0.02	2.76	−1.16	3.95	6.51	1.00	1.02(1.01)	105.8(106.7)	−0.09	−0.30	−0.9(100)	−0.2(0)
PH_3	−1.48	−3.82	0.36	1.97	−4.72	6.67	4.06	1.40	1.44(1.42)	92.5(93.3)	0.09	0.10	−1.9(94)	0.8(0)
AsH_3	−1.83	−5.27	0.96	2.49	−5.03	7.51	3.43	1.47	1.53(1.51)	90.7(92.0)	0.50	0.43	−2.1(94)	1.1(0)
SbH_3	−1.98	−4.43	1.16	1.28	−5.33	6.61	2.47	1.65	1.72(1.69)	90.7(91.5)	0.47	0.72	−2.1(95)	1.6(10)
BiH_3[c]	−2.70	−6.62	1.80	2.12	−5.89	8.00	1.40	1.72	1.82(1.81)	87.0(−)	0.34	0.70	−2.7(96)	2.3(4)
	[−2.55]	[−0.35]	[−0.08]	[−2.11]	[−8.11]	[6.00]								

[a] Experimental values of *R* and α are taken from ref 6 and the references therein. [b] The effective charges *q* of A^{III}, the metal ns and np contributions (in % electron density, in parentheses) to the a_1' and a_2'' HOMOs and LUMOs, and their energy changes during the $D_{3h}\rightarrow C_{3v}$ transition ($\delta E_{a2''}$, $\delta E_{a1'}$) are also listed. The energies listed for the fluorides in the second line are those with respect to the ionic fragments A^{3+} and F^- as the reference. For BiF_3 and BiH_3, the angular energy changes for $D_{3h}\rightarrow C_{3v}$, if the bond length is kept constant at R(D_{3h}), are also given (in brackets); here the energies of the radial changes in C_{3v} according to R(D_{3h})→R(C_{3v}) are obtained by subtracting the angular energies from those respresenting the total process. [c] The contributions $\delta E_{orb}(a_2)$ from the (nonbonding) $a_2(a_2')$ MO to δE_{orb} are very small or vanishing. [d] Here the HOMO is of a_2'' symmetry.

pair with directional p_z character away from the ligands. The Bi−F spacing in C_{3v} is slightly lower than the one estimated from reported ionic radii (≅2.1 Å),[26] whereas it is close to it in the D_{3h} complex. The neglect of relativistic corrections leads to a larger energy gain $\delta E_t = -1.73$ eV, because such correction contracts in particular the 6s electron clouds, thus enhancing the $A_1'(6s^2)-A_2''(6s^16p_z^1)$ energy separation Δ [eq 1] and reducing the extent of the lone pair effect. The inclusion of spin−orbit coupling yields only negligibly small changes of the Bi−F bonding energy, as expected for an "s^2" ground state. DFT calculations on TlF_3 yield the minimum at the D_{3h} geometry. The effective charge of Bi^{III} is about 1.8, indicating significant ionic bond contributions, and similar to that of Tl^{III} in TlF_3 (1.7). BiF_3 and TlF_3 are known as stable solids with interconnected polyhedra but are not observed as isolated species. The CN of Bi^{III} in the former solid crystallizing in the YF_3 structure is 8(+1).

The MO energies and their atomic orbital (AO) 6s,p(Bi) compositions for the D_{3h} geometry are depicted in Figure 2. The 6s(Bi^{III}) electron density distributes over the $5a_1'$ and $6a_1'$ MOs. Due to the energetic position of the fluorine 2p AOs being considerably higher than that of 6s, the HOMO $6a_1'$ is mainly ligand determined. In contrast, the antibonding $4a_2''$ LUMO is of dominating $6p_z$ character. A similar MO scheme is calculated for TlF_3, with $6a_1'$ being the LUMO in this case. In difference to BiF_3, the magnitudes of the metal 6s contributions to $5a_1'$ and $6a_1'$ are roughly reverse with 45% and 67%, respectively, due to the much higher position of the 6s AO of Tl in comparison to that of Bi. The calculated Tl−F bond length (Table 1) is somewhat larger than the one expected from reported ionic radii (≅1.95 Å[25]). Only two MOs of BiF_3 are strongly energetically affected by the symmetry decrease from D_{3h} to C_{3v} (Figure 2), namely $6a_1'$ and $4a_2''$. In accord with the one-electron aspect of the introduced vibronic coupling model ($a_1'\otimes\alpha_2''\otimes a_2''$ interaction), these are the MOs originating from the 6s and $6p_z$ Bi^{III} orbitals, which mix in the lower symmetry, yielding $9a_1$ and $10a_1$. The antibonding "lone pair" $9a_1$ MO is strongly stabilized, adopting 1/3 $6p_z$ character by the mixing process. The energy difference between the many electron ground state $A_1'[(6a_1')^2]$ and the first excited state $A_2''[(6a_1')^1(4a_2'')^1]$, which are involved in the $A_1'\otimes\alpha_2''\otimes A_2''$ PJT interaction, is $\delta \cong 3$ eV (Table 1). Without stressing the quantitative relevance of Kohn−Sham MO diagrams too much, it is quite clear, though, that the lone pair ($9a_1$) is predominantly localized on the ligand (Figure 2a) and not nonbonding with respect to the central ion, as is frequently claimed in the literature.

We deduce from the positive steric repulsion term (δE_P) and the negative covalent (δE_{orb}) and ionic (δE_{el}) energy contributions to the total energy change δE_t during the $D_{3h}\rightarrow C_{3v}$ transition for BiF_3 (Table 1), the latter two overcompensating the former, that it is the stronger bonds that stabilize the C_{3v} with respect to the D_{3h} geometry. If one roughly correlates δE_P with the energy contribution, which is supposed to be the driving force for the symmetry change in the VSEPR model (see section II), minimum steric repulsion between the strongly delocalized 6s/6p lone pair (Figure 2a) and the Bi−F bonding electron pairs does not occur in the optimized C_{3v} geometry, in contrast to the expectation assuming the validity of the VSEPR concept. Table 1 gives also the contributions to δE_{orb}, which stem from the energetic changes of the a_1', a_2'' to the a_1 MOs and of the e',e'' to the e MOs, respectively, during the $D_{3h}\rightarrow C_{3v}$ transition. It is quite clear from these numbers that $\delta E_{orb}(a_1)$ controls δE_t in the case of BiF_3. More specifically, the Kohn−Sham MO scheme (Figure 2, Table 1) gives evidence that δE_t (≅ −1.2 eV) is predominantly determined by the energetic stabilization of the $6a_1'$ MO ($2x\delta E_{\alpha 1'} = -1.6$ eV). Calculations with ionic fragments, namely Bi^{3+} and F^- as the reference instead of Bi^0 and F^0, lead to essentially the same conclusions, though the magnitudes of the various energy contributions to δE_t change significantly. We have listed these values as well, because the effective charges of the metal ion in BiF_3 (and SbF_3, AsF_3) are the highest of all investigated molecules − more than intermediate between "Bi^0" and "Bi^{3+}" (Table 1).

We further note that, when calculating the vibrational energies

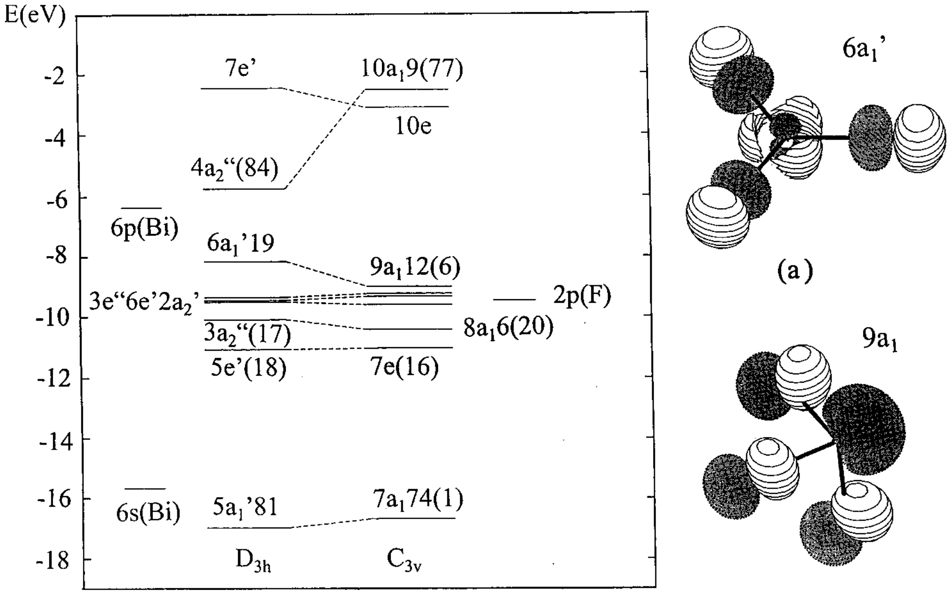

Figure 2. MO scheme of BiF_3 for DFT optimized D_{3h} and C_{3v} geometries with the 6s and 6p (in parentheses) metal contributions (%) indicated (left). The symmetry-adapted LCAOs in D_{3h} originating from the ligand 2s and 2p orbitals are a_1',$e'(\sigma)$ and $a_1'(\sigma)$; $2xe'(\sigma,\pi$ in plane); $a_2''(\pi$ out-of-plane); a_2', e'' (nonbonding). The metal 6s and 6p AO's transform as $a_1'(\sigma)$ and $a_2''(\pi$ out-of-plane), $e'(\sigma,\pi$ in-plane). The low lying $4a_1'$ and $4e'$ MOs at $\cong -28$ eV are nearly nonbonding with respect to the ligand 2s orbitals and not drawn. The approximate energies of the parent Bi(6s,6p) and ligand F(2s,2p) orbitals for effective charges of Bi and F in D_{3h} (Table 1) were calculated making use of the Kohn–Sham orbital energies and eigenfuctions. Figure 2a illustrates the wave function (ψ) underlying the "lone pair" HOMO of BiF_3 in D_{3h} (above) and C_{3v} (below), predominantly delocalized toward the ligand (right). The contour plot diagram is constructed for ±0.06 values of ψ. Small 5d contributions from the Bi core are also seen.

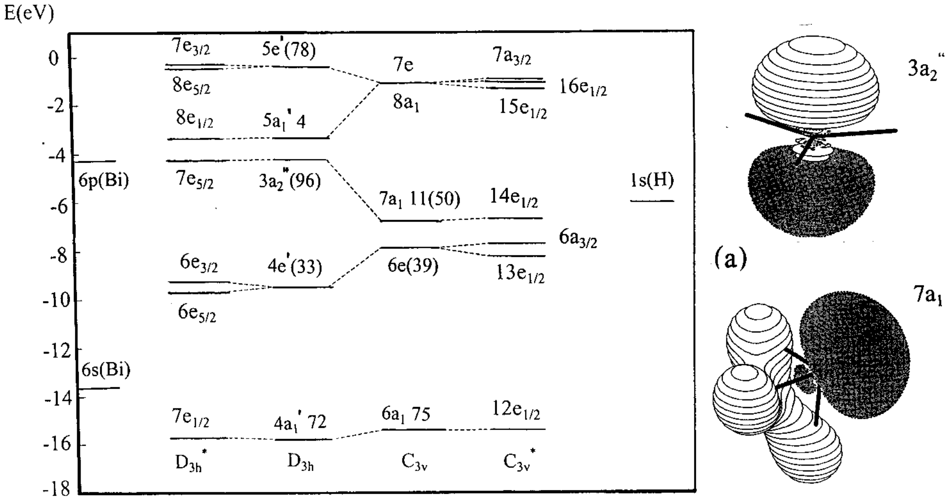

Figure 3. MO scheme of BiH_3 for DFT optimized D_{3h} and C_{3v} geometries, with the metal 6s and 6p (in parentheses) contributions (%) indicated (left). The symmetry-adapted LCAOs in D_{3h} stemming from the ligand 1s orbitals are $a_1'(\sigma)$ and $e'(\sigma)$, while the metal 6s and 6p orbitals transform as $a_1'(\sigma)$, $e'(\sigma)$ and a_2''(nonbonding). The energies of the parent metal Bi(6s,6p) and H(1s) ligand orbitals for the Bi and H effective charges in D_{3h} (Table 1) were estimated making use of the Kohn–Sham orbital energies and eigenfuctions. Additionally, the MO splittings by spin–orbit coupling (symmetry notations according to the D_{3h}* and C_{3v}* double groups) are shown. Figure 3a illustrates the wave function (ψ) underlying the "lone pair" HOMO of BiH_3 in D_{3h} (above) and C_{3v} (below). The contour plot diagram is constructed for ±0.06 values of ψ. Small 5d contributions from the Bi core are also seen.

of BiF_3 in D_{3h} in comparison to those of TlF_3 (see Table 4), the α_2'' vibration possesses a "negative" enegy (imaginary frequency) for BiF_3, thus giving direct evidence for the geometric instability of the D_{3h} structure with respect to C_{3v}.

If a ligand is chosen which lacks π-bonding abilities, a new feature comes into play. The MO scheme calculated for such a case, namely BiH_3, is depicted in Figure 3 (see the intermediate section – D_{3h}, C_{3v}). Because the $3a_2''$ MO originating from $6p_z$ is nonbonding in D_{3h}, it is located energetically below the σ-antibonding $5a_1'$ level. Thus we have a reverse situation as compared to BiF_3 (Figure 2), with a metal $(6p_z)^2$ based HOMO (Figure 3a) and a LUMO $5a_1'$, which is nearly completely ligand-centered. The A_1' ground state originates from $(3a_2'')^2$, and the first excited-state A_2'' stems from $(3a_2'')^1(5a_1')^1$. Also in this case, significant energy changes, which involve the $3a_2''$ and $5a_1'$ MOs, arise when lowering the symmetry from D_{3h} to C_{3v}. They are accompanied by an admixture of about 20% metal 6s character and a large increase of the ligand contributions to the HOMO (Figure 3a: $7a_1$), in which the lone pair resides. However, additional very distinct positive energy shifts of the e' MOs, in particular for the occupied $4e'$, occur. This result is reflected by the $\delta E_{orb}(a_1)$ and $\delta E_{orb}(e)$ contributions, from which the latter is strongly positive, making δE_{orb} also positive (Table 1).

More insight into the bonding situation for BiF_3 and BiH_3 is gained if one separates the energy effects into the radial and angular components (Table 1). While δE_P and δE_{el} result nearly exclusively from the bond length variation, the covalent bond energies δE_{orb} and $\delta E_{orb}(a_1)$, $\delta E_{orb}(e)$ are influenced by both radial and angular changes in a rather complex manner. $\delta E_{orb}(e)$ possesses positive angular components, due to the loss of σ overlap for the $6p_{x,y}$ orbitals by the geometry change, which is partly compensated by π-bonding in the case of BiF_3. $\delta E_{orb}(a_1)$ [angular] has a large negative energy for BiF_3 and BiH_3, indicating that the stabilization energy of the MOs involved in the $D_{3h} \rightarrow C_{3v}$ vibronic coupling process is of dominant importance. The energy stabilization is enlarged in the case of BiF_3 and reduced for BiH_3 by the radial effect ($\delta E_{orb}(a_1)$ [radial], $\delta E_{orb}(e)$ [radial] < 0 and > 0, respectively; see Table 1). It is finally interesting to note that, when adding up the various energy contributions, δE_t turns out to be an angular energy in very good approximation.

After all, the changes of the bonding parameters during the $D_{3h} \rightarrow C_{3v}$ transition calculated for BiH_3 are *reverse* to those for BiF_3. The steric repulsion δE_P is negative for BiH_3 with a "p_z^2" groundstate ($dR > 0$) and positive for BiF_3 ("s^2" ground state; $dR < 0$) and predominantly caused by the radial bond length variation dR (δE_P[angular] is very small). *Apparently, it is not the forces underlying the VSEPR model, even in the case of BiH_3, which stabilize the distorted geometry but the improved overlap particularly within the HOMO.* The total covalent bond energy changes δE_{orb} are positive and negative for BiH_3 and BiF_3, respectively, and are sensitive to both the angular and radial geometry variation.

BiH_3 is known as gaseous compound, which has not been structurally characterized, however. The DFT calculations for TlH_3 yielded a positive energy E_t. δE_t for BiH_3 is calculated to be much larger when accounting for scalar relativistic effects [-2.70 eV (Pauli) or -2.64 eV(ZORA)] as compared to the nonrelativistic result [-1.77 eV], just opposite to the BiF_3 case. This is readily explained by the particularly distinct relativistic contraction of the 6s orbital, which reduces considerably the $6s-6p_z$ separation energy. Whereas the relativistic contraction is more pronounced for BiH_3 than for BiF_3, the additional consideration of spin−orbit coupling yields again only negligible energy changes ($\delta E_t = -2.59$ eV, ZORA calculation), though the spin−orbit coupling constant for Bi^{3+} is rather large (0.8 eV). Apparently the orbital momentum of the 6p orbitals in BiH_3 is largely suppressed, because the total bonding energy clearly dominates the spin−orbit coupling effect, in accordance with the Van-Vleck theorem. The effect of the spin−orbit interaction is illustrated by the orbital energy diagram in Figure 3, employing D_{3h}* and C_{3v}* double group symmetries.

2. AF_3 and AH_3 Molecules (A^{III} = N, P, As, Sb). In Table 1 we have listed the calculated energy and geometrical parameters for the fluorides and hydrides of the fifth main group elements from N to Bi. The comparison of the bond lengths and angles with experimental structural data yields generally a rather good agreement for the bond angles, while the calculated A−X spacings are somewhat larger than the reported ones, particularly in the case of the fluorides. As expected, the DFT results of the AH_3 molecules resemble those of BiH_3, with a HOMO corresponding to a nonbonding np_z electron pair [$(a_2'')^2$] and a LUMO, which is predominantly or completely ligand centered. Again, the covalent bond energy δE_{orb} is positive due to the large $\delta E_{orb}(e)$ contribution, which indicates a significant destabilization of the e MOs originating from the A^{III} $np_{x,y}$ orbitals during the transition from D_{3h} to C_{3v}, as discussed for BiH_3 already. The driving forces for the symmetry break are the steric repulsion energy due to the widening of the AH bond lengths on one hand and the contribution to δE_{orb} stemming from the a_1 MOs on the other, as will be further discussed in some detail later.

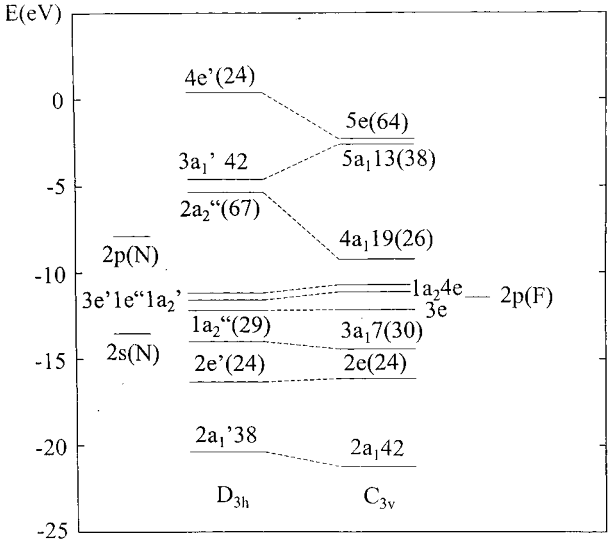

Figure 4. MO scheme of NF_3 for DFT optimized D_{3h} and C_{3v} geometries. Energy levels for the *N*(2s,2p) and *F*(2p) atomic orbitals were calculated making use of the Kohn−Sham orbital energies and eigenfuctions.

The fluorides AF_3 behave similar to BiF_3 in possessing a strongly delocalized HOMO (a_1') and a metal-centered LUMO (a_2''), though the central atom character of the HOMO is larger (Table 1). An exception is NF_3, where a reverse MO sequence is found, with the lone pair residing predominantly in the a_2'' MO, as was known before.[6] The reason can be taken readily from the MO scheme of NF_3 (Figure 4) in comparison to those of the other fluorides, which resemble that of BiF_3 (Figure 2). The σ- and π-antibonding effects of the HOMO and LUMO, as measured by the energy of these MOs with respect to the atomic 2p(F) and np_z(A) AOs, respectively, both increase steadily from BiF_3 to PF_3, the σ effect being much more distinct, however, as expected. Proceding from PF_3 to NF_3 a further steep increase occurs, leading to an "overtaking" of the a_1' HOMO by the a_2'' LUMO. This phenomenon is nicely imaged by the LUMO−HOMO separations δ' or the corresponding many-electron term δ [Table 1 − analogous to Δ in matrix (1), see section IV]. δ' (a_1' being the reference) decreases from BiF_3-($\cong$2.4 eV) to PF_3 ($\cong$1.5 eV), becoming negative in the case of NF_3 ($\cong -0.8$ eV). The reverse trend is observed in the MH_3 series: δ' (a_2'' being the reference), which measures solely the σ-antibonding character of the LUMO in this case, because the lone pair is nonbonding, increases from Bi to N, with larger jumps from Bi to Sb, and particularly from P to N. The comparatively large δ' and δ changes from $BiF(H)_3$ to $SbF(H)_3$ are due to relativistic effects; the shrinking of the 6s orbital reduces the extent of σ-antibonding of the a_1' HOMO(LUMO), thus enhancing (reducing) δ, δ' particularly for Bi^{III}. The singular position of nitrogen in the series from Bi^{III} to N^{III} is clearly due to the drastically enhanced covalency of the N−F(H) bond (see Appendix). This is indeed reflected by an increase of the negative E_{orb} contribution to E_t in D_{3h} by $\cong$18(20) eV, proceding from P^{III} to N^{III}. In comparison, the corresponding value for the range from Bi^{III} to P^{III} is only $\cong$13 (11) eV. The fluorides of P^{III}, As^{III}, and Sb^{III} possess, similar to BiF_3, negative δE_{orb} and δE_{el} energies, indicating a strengthening of both the covalent and ionic central atom-ligand interactions in C_{3v}. Here the large

TABLE 2: Proton Affinities (eV) for AX_3 Molecules before (E_a^o) and after Relaxation into the Final Geometry (E_a), and Available Experimental Energies (E_a^{exp})[a]

	E_a^o	E_a	E_a^{exp}	ΔR	$\Delta\alpha$	Δ_s	%p (%s)
NH_3	−9.0	−9.1	−9.0	0.01	3.8	−0.9	80(10)
PH_3	−7.5	−8.1	−8.2	−0.02	17.2	−1.9	63(19)
AsH_3	−7.1	−7.8	−7.8	−0.04	18.7	−2.2	60(16)
SbH_3	−7.1	−7.8		−0.05	20.5	−2.1	54(18)
BiH_3	−6.3	−7.1		−0.07	22.5	−2.7	49(11)
NF_3	−5.5	−6.0	−6.3	−0.06	7.1	−3.9	26(19)
PF_3	−5.6	−6.5	−7.2	−0.09	11.1	−1.4	23(38)
AsF_3	−4.4	−5.0		−0.08	10.4	−1.3	16(30)
SbF_3	−4.2	−4.8		−0.07	11.6	−1.4	14(26)
BiF_3	−3.2	−3.5		−0.06	9.2	−0.8	6(12)

[a] The corresponding angular ($\Delta\alpha$ in degrees) and radial changes (ΔR in Å) are also listed. Δ_s (= $\delta Ea1'$ or $\delta Ea2''$ (in eV) see Table 1) is the HOMO stabilization during the D_{3h}→C_{3v} transition of the AX_3 molecules and %p (%s) gives the percentage of metal p_z(s) character in the HOMO in the C_{3v} geometry.

negative $\delta E_{orb}(a_1)$ energy controls the total energy gain δE_t. $\delta E_{orb}(e)$ is positive and rather small, because the loss of σ-overlap for the $p_{x,y}$ orbitals by the symmetry reduction from D_{3h} to C_{3v} is almost compensated by the shrinking of the M−F bond by 0.08(2) Å (Table 1). NF_3, with an effective charge of N rather near to the atomic fragment reference, behaves as the hydrides in that repect; the increase of the bond length induces a considerable destabilization of the e-MOs as indicated by a strongly positive $\delta E_{orb}(e)$ energy, which compensates the negative δE_P contribution (see the discussion of BiH_3 in section III.1). Though the energy changes δE_P, δE_{el}, δE_{orb}, $\delta E_{orb}(a_1)$, and $\delta E_{orb}(e)$ are considerably different, using ionic fragments M^{3+} and F^- as the reference (in particular in the case of NF_3), the general conclusion remains. In the case of a ($a_2''^2$), ground state δE_P and $\delta E_{orb}(a_1)$ determine the sign of δE_t, while for a ($a_1'^2$) ground state it is $\delta E_{orb}(a_1)$ together with the ionic δE_{el} contribution, which makes δE_t negative.

It is tempting to find a correlation between the electronic properties and the base character of the molecules under consideration. We propose that the donor properties are the more distinct, the more p_z character the lone pair possesses, because the directional property of this orbital is expected to control the availability of the lone pair for an overlap with an acidic reactant. The experimental proton affinities E_a, deduced from pulsed high-temperature mass spectrometry,[27] and the results of DFT calculations for the gas-phase reaction

$$AX_3 + H^+ \rightarrow AX_3H^+ \text{ (X:F,H)}$$

show indeed, that such a simple concept might be valid (Table 2). Two different types of calculations have been performed. When evaluating E_a^o, the equilibrium geometries resulting from geometry optimizations of the free AX_3 molecules have been fixed, adjusting only the "$A-H^+$" bond length. E_a^o may be considered to directly probe the availability of the lone pair. E_a is the proton affinity with the fully optimized AX_3H^+ cation as the final state. In all cases, the energy minima occur at $T_d(AH_4^+)$ and $C_{3v}(AF_3H^+)$. The calculated proton affinities are in close agreement with available experimental data and indeed follow nicely the p_z percentage of the lone pair (Table 2). The weaker base properties of NF_3, as compared to PF_3, could be caused by the very large HOMO stabilization $\delta E_{\alpha 2''}$ (Table 1) of the former molecule when lowering the symmetry from D_{3h} to C_{3v}, thus leading to a shrinking of the lone pair and to less pronounced donor properties.

It is not possible at the present stage of discussion to find a simple correlation between the energy stabilization δE_t and the geometrical changes, namely the angular and bond length variations, during the D_{3h}→C_{3v} transition, which is based on a nonsophisticated and easily accessible concept. Thus, while in the fluoride series the stabilization energies $|\delta E_t|$ decrease with increasing deviations from the planar geometry, the opposite is the case for the hydrides. We will show in section IV that the vibronic coupling model is able to rationalize even such controversial behavior utilizing involved vibronic coupling and force constants.

3. AX_3 Molecules (A^{III}: N to Bi; X^{-I}: Cl, Br, I). Table 3 summarizes the calculated energy and geometrical parameters for the chlorides, bromides, and iodides, which may be readily compared with the analogous properties of the fluorides and hydrides (Table 1). The derived bond angles are mostly very close to the experimental ones, whereas the calculated M−X spacings are generally larger than those from experiment by about 0.06 Å, but without inconsistencies in the trends. An interesting, but not unexpected observation is that NCl_3 and NBr_3 have a A_1' ($a_2''^2$) ground state as NF_3, with a decreasing energetic distance δ to the excited A_2'' ($a_2''^1 a_1'^1$) state, however, proceding from F^- to Br^-. In the case of NI_3, the HOMO−LUMO separation is nearly vanishing. Here, an $A_2''(a_1'^1 a_2''^1)$ ground state is calculated in D_{3h}, with very close-lying excited $A_1'(a_1'^2)$ and $A_1'(a_2''^2)$ states in energetic distances of ≈0.1 eV and ≈0.4 eV, respectively. In view of this, a multiconfiguration SCF treatment would be the proper calculational choice for NI_3. In difference to the hydrides and NF_3 (Table 1), it is solely the strongly negative steric repulsion, due to the extension of the N−Br(Cl) bond length (for example NBr_3: $\delta E_p[\text{radial}] = -11.97$ eV), which stabilizes the distorted geometry of the molecules NX_3 (X=Cl,Br). Nevertheless, the HOMO stabilization energy $\delta E_{a2''}$ is distinctly negative in these cases, even though $\delta E_{orb}(a_1)$ is slightly positive or vanishing (Table 3). We will discuss this point in greater detail in the next section. The molecules AX_3, with A: P to Bi and X: Cl, Br, I, possess energetic properties analogous to the corresponding fluorides with the same $A_1'(a_1'^2)$ ground states ($\delta E_P > 0$; δE_{orb}, $\delta E_{el} < 0$). Looking at the angular and radial changes separately, as has been done for BiH_3 and BiF_3 (section III.1; Table 1), we note an analogous behavior; δE_P and δE_{el} are sensitive to the bond length variation nearly exclusively, whereas the δE_{orb} energies and their a_1 and e components reflect both the angular and radial changes (model calculations for NBr_3 and PCl_3).

In Table 4 we have listed the ground-state vibrational energies calculated at D_{3h} and C_{3v} stationary points with the bond lengths and bond angles deduced from the geometry optimization (Table 3), including also the data for the fluorides and hydrides (Table 1). As follows from the positive vibrational energies, absolute minima at C_{3v} geometries result for all molecules under consideration. In general there is reasonable agreement between experimental and DFT vibrational energies, the calculated values for the halides being lower than the experimental energies. This is the opposite to the results of Hartree−Fock and MP2 methods which overestimate the vibrational energy. D_{3h} stationary points are always characterized by negative α_2'' frequencies corresponding to a saddle point of the ground-state potential curve (negative force constant; see Figure 5b). The magnitudes of the negative α_2'' energies decrease more distinctly than the other vibrational energies when proceeding from N to Bi in the case of the halides, indicating less distinct vibronic instabilities. The reversed behavior in the case of the hydrides finds its explanation by initial $A_1'-A_2''$ separations δ, which increase considerably in the sequence from Bi to N (Table 1) and hence weaken

TABLE 3: Calculated Energies [δE_t, δE_P, δE_{el}, δE_{orb} and Its Components from the $a_1(a_1',a_2'')$ and $e(e',e'')$ MOs, δ − $(A_2''-A_1')$ Separation, in eV] and Geometrical Parameters (Bond Lengths *R* in Å and Angles α in degrees, experimental values[a] in parenthesis) for Molecules MX_3 (M^{III}: N to Bi and Tl; X^-: Cl, Br,I)[b]

	δE_t	δE_P	δE_{el}	δE_{orb}	$\delta E_{orb}(a_1)$	$\delta E_{orb}(e)$	δ	$R(D_{3h})$	$R(C_{3v})$	$\alpha(C_{3v})$	$q(D_{3h})$	$q(C_{3v})$	$\delta E_{a2''}$(%M)	$\delta E_{a1'}$(%M)
NCl_3	−1.02	−14.89	4.34	9.53	0.65	8.83	1.07[c]	1.70	1.81(1.76)	107.4(107.3)	−0.27	−0.18	−1.9(47)[c]	−0.4(17)
PCl_3	−1.86	9.73	−3.72	−7.87	−6.60	−1.31	0.93	2.22	2.10(2.05)	101.0(100.1)	0.27	0.07	3.0(64)	−0.8(18)
$AsCl_3$	−1.41	6.94	−2.80	−5.56	−5.37	−0.22	1.40	2.31	2.22(2.16)	100.4(98.9)	0.57	0.42	2.6(66)	−0.7(13)
$SbCl_3$	−1.30	5.91	−2.47	−4.74	−4.86	0.10	1.53	2.48	2.40(2.33)	99.4(97.2)	1.07	1.04	2.6(71)	−0.6(16)
$BiCl_3$	−0.90	3.90	−1.71	−3.09	−4.18	1.05	2.01	2.55	2.48(2.42)	97.3(97.3)	1.14	1.07	2.2(72)	−0.4(8)
$TlCl_3$								2.40		120	0.90		(91)	(44)
NBr_3	−1.09	−11.28	3.67	6.53	0.00	6.47	0.41[c]	1.87	1.98	108.1	−0.37	−0.22	−1.7(48)[c]	0.1(13)
PBr_3	−1.46	7.22	−3.03	−5.66	−4.89	−0.81	0.83	2.38	2.28(2.22)	102.2(101.0)	0.41	0.21	2.2(60)	−0.7(13)
$AsBr_3$	−1.14	5.22	−2.31	−4.05	−4.11	0.02	1.22	2.47	2.39(2.33)	101.7(99.9)	0.67	0.53	2.0(62)	−0.5(10)
$SbBr_3$	−1.10	4.89	−2.22	−3.77	−3.96	0.16	1.34	2.64	2.55(2.49)	100.6(98.2)	1.11	1.11	2.1(67)	−0.5(12)
$BiBr_3$	−0.80	3.20	−1.54	−2.46	−3.59	1.07	1.77	2.69	2.63(2.63)	98.0(100.0)	1.15	1.10	1.9(69)	−0.3(6)
$TlBr_3$								2.55		120	0.93		(88)	(37)
NI_3	−0.70	−0.47	−0.03	−0.20	−1.40	1.18	*c*	2.16	2.17	110.9	−0.86	−0.80	−0.8(43)[c]	0.2(6)
PI_3	−1.16	5.72	−2.59	−4.30	−3.69	−0.65	0.64	2.60	2.50(2.46)	103.4(102)	−0.04	−0.36	1.6(55)	−0.6(8)
AsI_3	−0.92	4.30	−2.05	−3.17	−3.22	0.02	0.97	2.68	2.60(2.56)	102.7(100.2)	0.12	−0.15	1.4(58)	−0.5(6)
SbI_3	−0.83	3.87	−1.89	−2.82	−2.95	0.12	1.07	2.87	2.79(2.72)	102.8(99.0)	0.55	0.43	1.4(61)	−0.4(7)
BiI_3	−0.62	2.28	−1.21	−1.69	−2.81	1.08	1.41	2.92	2.87(2.81)	99.4(99.5)	0.67	0.59	1.3(62)	−0.2(3)
TlI_3								2.76		120	0.37		(91)	(28)

[a] Experimental values of R and α are taken from ref 6 and the references therein. [b] The effective charges *q* of M^{III}, the energy changes $\delta E_{a2''}$, $\delta E_{a1'}$ of the HOMOs and LUMOs during the $D_{3h}\rightarrow C_{3v}$ transition and the metal ns and np_z contributions to the HOMOs and LUMOs (in % electron density, in parentheses) are also listed. [c] $A_1'(a_2''^2)$ and $A_2''(a_2''^1a_1'^1)$ ground states for NCl_3, NBr_3, and NI_3, respectively (see text).

TABLE 4: Calculated Vibrational Energies (in cm^{-1}, DFT, spin-restricted calculations) for AX_3 Molecules (A=N,P,As,Sb,Bi[a] and X=H,F,Cl,Br,I) in Their Ground State Configuration and Experimental Values[a] (calculated values for TlX_3 compounds also listed)[b]

		H			F			Cl			Br			I		
	$\nu_{D3h(C3v)}$	D_{3h}	C_{3v}	exp.	D_{3h}	C_{3v}	exp.	D_{3h}	C_{3v}	exp.	D_{3h}	C_{3v}	exp.	D_{3h}	C_{3v}	exp.
N	$\alpha_1'(\alpha_1)$	3545	3377	3337	782	997	1032	448	565	540	268	469		*c*	358	
	$\epsilon'(\epsilon)$	1513	1628	1628	410	446	493	250	224	258	146	131		*c*	85	
	$\epsilon'(\epsilon)$	3752	3497	3414	1235	810	908	833	536	643	709	475		*c*	408	
	$\alpha_2''(\alpha_1)$	−799	1040	950	−1113	598	647	−518	316	349	−501	190		*c*	131	
P	$\alpha_1'(\alpha_1)$	2486	2285	2321	540	805	892	320	481	512	196	369	390	131	278	303
	$\epsilon'(\epsilon)$	965	1072	1121	−174	294	347	−54	163	187	−20	98	113	21	62	79
	$\epsilon'(\epsilon)$	2580	2310	2248	610	772	860	392	466	505	334	373	384	278	298	325
	$\alpha_2''(\alpha_1)$	−1043	984	991	−478	413	488	−335	227	260	−278	142	160	−214	93	111
As	$\alpha_1'(\alpha_1)$	2344	2083	2122	549	678	741	317	389	424	194	272	290	128	195	218
	$\epsilon'(\epsilon)$	899	990	1005	−93	229	262	12	132	153	20	82	93	17	54	67
	$\epsilon'(\epsilon)$	2415	2105	2185	525	641	702	318	361	398	249	266	284	197	205	222
	$\alpha_2''(\alpha_1)$	−1130	915	906	−313	296	336	−206	169	194	−159	112	125	−121	77	92
Sb	$\alpha_1'(\alpha_1)$	2092	1873	1891	523	612	654	300	354	381	184	241	256	118	164	
	$\epsilon'(\epsilon)$	707	818	831	−31	174		−22	114	122	−9	70	76	17	47	55
	$\epsilon'(\epsilon)$	2162	1903	1894	512	593	624	294	327	359	217	226	249	164	162	194
	$\alpha_2''(\alpha_1)$	−1052	778	782	−227	216	259	−173	143	151	−133	94	101	−96	66	74
Bi	$\alpha_1'(\alpha_1)$	1900	1742	1760	506	568		297	331	342	184	218	220	120	146	
	$\epsilon'(\epsilon)$	617	777	750	66	158		−47	97	107	13	62	63	23	41	47
	$\epsilon'(\epsilon)$	1993	1749	1770	484	538		293	305	332	200	206	214	146	145	164
	$\alpha_2''(\alpha_1)$	−1666	767	720	−192	180		−131	113	123	−90	76	77	−70	54	60

[a] Experimental vibrational frequencies are taken from Ref.[6] and cited references; [b] The calculated α_1', ϵ', ϵ', α_2'' (D_{3h}) vibrational energies for TlF_3, $TlCl_3$, $TlBr_3$ and TlI_3 are 517, 72, 524,129 cm^{-1}; 296, 69, 320, 84 cm^{-1}; 180, 46, 219, 63 cm^{-1}; and 111, 35, 154, 63 cm^{-1} respectively; [c] $A_2''(a_1'^1a_2''^1)$ ground state.

the vibronic interactions. In contrast, TlX_3 (X=F,Cl,Br,I) molecules are stable in D_{3h}, as expected.

In some cases, in particular for PF_3 and AsF_3, negative values are calculated for the predominantly angular ϵ' vibration in D_{3h} also. Indeed, a second type of PJT distortion may occur in D_{3h}, which couples the $6a_1'(6s)$ with the $7e'(6p_{x,y})$ MO via the two ϵ' vibrational modes, leading to an in-plane C_{2v} distortion. Because the lowest-energy empty e′ MO is much higher in energy than the a_2'' or a_1' LUMO (Figures 2, 3, 4) and the respective coupling constant rather small, this interaction is not however, of steric relevance (for a more thorough discussion of this effect, see ref 6b). This is evidenced by the energies of the ϵ modes in C_{3v} which are all positive. It should be mentioned further that a positive vibrational energy is calculated in all cases for the α_2'' mode in the excited A_2'' state in D_{3h} (not listed in Table 4). Accordingly, geometry optimizations of the first excited state, starting from the C_{3v} geometry, usually relax to the D_{3h} molecular structure. However, the hydrides from PH_3 to BiH_3, as well as NF_3 and PF_3, exhibit negative values for the angular ϵ' mode in D_{3h}; in these cases the planar C_{2v} structure is the stable excited-state geometry. This finding might lead to interesting effects in spectroscopy, producing increased Stokes' shifts between absorption and emission bands.[28] We neglect this finer effect in the following.

IV. Which Bonding Parameters Determine the Energetic and Geometric Changes along the $D_{3h}\rightarrow C_{3v}$ Distortion Pathway?

We will demonstrate in this section that a vibronic coupling model, in an effective sense, is able to rationalize and

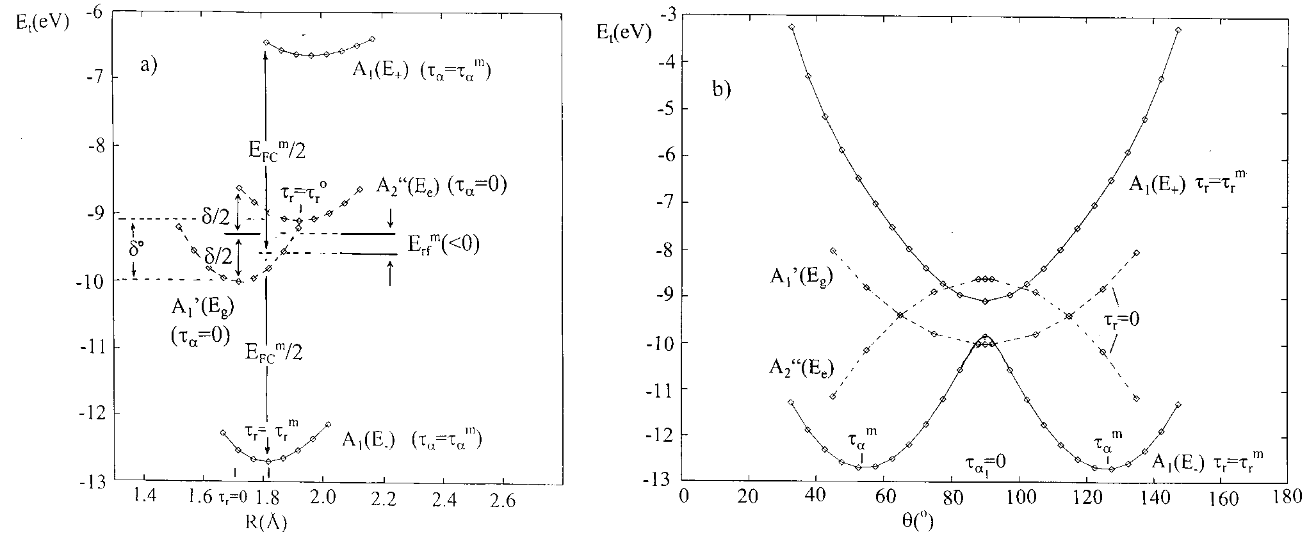

Figure 5. (a) Ground state and excited state potential curves $A_1(E_-)$, $A_1(E_+)$, DFT optimized in the C_{3v} geometry and projected onto the $E-\tau_r$ plane at τ_α^m (full lines). Projections at $\tau_\alpha = 0$ (D_{3h}) of the same curves [$A_1'(E_g)$, $A_2''(E_e)$, hatched lines] are also shown. The energy separations δ^o, δ, E_{FC}^m, and the restoring energy E_{rf}^m, as well as the optimized τ_r^o and τ_r^m displacements with respect to the $A_1'(E_g)$ minimum position ($\tau_r = 0$), which is the reference ($E = 0$) for the energy scale, are also marked [eqs 5, 7, 8)]. (b) The angular dependencies of the $A_1'(E_g)$ and $A_2''(E_e)$ potential surfaces at $\tau_r = 0$ (hypothetical, see text; hatched curves) and of the final $A_1(E_-)$ and $A_1(E_+)$ states at $\tau_r = \tau_r^m$ (compare with Figure 1). The given numerical values are those for BiH_3.

systematize calculational and experimental results, which are sometimes contradictory at the first sight. Considerations on the basis of such concept yield a simple and clear dependence of the geometric and energetic changes during the $D_{3h}\rightarrow C_{3v}$ transition on certain effective vibronic coupling parameters and force constants.

1. The Vibronic Coupling Model for MX$_3$ Molecules. The DFT calculations have shown, that the angular changes characterizing the D_{3h} to C_{3v} transition of AX_3 molecules are always accompanied by significant changes of the A−X bond lengths. This means that the vibronic treatment has to include the coupling to the totally symmetric α_1' mode [$A_1'\otimes(\alpha_1' + \alpha_2'')\otimes A_2''$ interaction] and that matrix (1) has to be extended accordingly [eqs 5].

$$\begin{array}{c} \begin{array}{cc} A_1(A_1') & A_1(A_2'') \end{array} \\ \begin{bmatrix} E_g-E & N \\ N & E_e-E \end{bmatrix} \end{array} \tag{5a}$$

$$E_g = (1/2)K_r\tau_r^2 + (1/2)K_\alpha\tau_\alpha^2 \tag{5b}$$

$$E_e = (1/2)K_r'(\tau_r - \tau_r^o)^2 + (1/2)K_\alpha'\tau_\alpha^2 + \delta^o$$

$$\delta E_{g,e} \equiv E_e - E_g = (1/2)(K_r' - K_r)\tau_r^2 + (1/2)(K_\alpha' - K_\alpha)\tau_\alpha^2 - K_r'\tau_r^o\tau_r + \delta \text{ with } \delta \equiv \delta^o + (1/2)K_r'\tau_r^{o2}$$

$$N = t_\alpha\tau_\alpha + t_{\alpha r}\tau_r\tau_\alpha$$

$$E_\pm = (1/2)\{E_g + E_e \pm [\delta E_{g,e}^2 + 4N^2]^{1/2}\}$$

$$E_{FC} \equiv E_+ - E_- = [\delta E_{g,e}^2 + 4N^2]^{1/2}$$

The parameters for the angular and bond length (radial) distortions τ_α and τ_r, corresponding to the α_2'' and the totally symmetric α_1' vibration, respectively, are defined by eq 6a; here θ (in degrees) or 180° − θ is the angle between the A−X bond vectors and the normal to the X_3-plane and connected with the XAX bond angle α by relation (6b).

$$\tau_r = \sqrt{3}\,[R(C_{3v}) - R(D_{3h})] \tag{6a}$$

$$\tau_\alpha = \sqrt{3}\,R(D_{3h})[\theta\,(C_{3v}) - \theta\,(D_{3h})](\pi/180)$$

$$\sin\theta = (2/\sqrt{3})\sin(\alpha/2) \tag{6b}$$

τ_r^o is the radial displacement in D_{3h} of the excited-state potential curve with respect to that of the ground state. K_r,K_α and K_r',K_α' are the force constants in the ground and the excited state. t_α is the first-order vibronic coupling constant responsible for the $D_{3h}\rightarrow C_{3v}$ symmetry break and $t_{\alpha r}$ a second-order coupling parameter; the latter together with the displacive terms connected with K_r, K_r' and τ_r allows for the energy changes as the consequence of the metal−ligand bond expansion or contraction, which accompanies the displacement along the α_2'' distortion path. E_- and E_+ are the solutions of determinant eq 5a, and E_{FC} [eq 5b], when calculated at the ground-state equilibrium geometry in C_{3v} (E_{FC}^m) [eq 8b], is the Franck−Condon transition energy and corresponds roughly to the maximum of the lowest electronic absorption band in spectroscopic experiments.[28] Equations 7 give two useful simplified relations for the ground-state energy E_- in the case of small nondiagonal energies, which can be readily compared with the expression in eq 2b.

$$N^2 \ll \delta E_{g,e}^2/4 \qquad E_- \cong E_g - N^2/\delta E_{g,e}, \text{ and with } \tau_r = 0,\ K_\alpha = K_\alpha': \tag{7a}$$

$$(t_\alpha\tau_\alpha)^2 \ll \delta^2/4 \qquad E_- \cong (1/2)K_\alpha^{vib}\tau_\alpha^2 \quad (K_\alpha^{vib} \equiv K_\alpha - 2t_\alpha^2/\delta) \tag{7b}$$

Figure 5a displays projections of the final ground-state $A_1(E_-)$ and excited-state $A_1(E_+)$ potential surfaces onto the $E - \tau_r$ plane (full curves), the angular coordinate corresponding to the minimum position τ_α^m in C_{3v} [see eq 8b]; the $A_1'(E_g)$ and $A_2''(E_e)$ potential curves (hatched) are those at $\tau_\alpha = 0$ (D_{3h}). The former two curves drawn for $\tau_\alpha = 0$ are identical with those of $A_1'(E_g)$ and $A_2''(E_e)$, because the vibronic coupling introduced by the nondiagonal term $t_{\alpha r}\tau_\alpha\tau_r$ in eqs 5 will change the force constants K_r and K_r' only along the τ_α coordinate. In Figure 5b, the angular dependence of the $A_1'(E_g)$ and $A_2''(E_e)$ potential curves at $\tau_r = 0$ is shown (hatched curves), having in mind that the corresponding force constants K_α (>0) and K_α'(<0) are hypothetical. They are strongly modified by the vibronic coupling along the α_2'' displacement path, and it is explicitly the cross-term N in eq 5b that induces K_α' to become positive and K_α negative in the final $A_1(E_-)$ and $A_1(E_+)$ states, respectively (full curves). This is nicely illustrated by eqs 7, valid in the vicinity of the D_{3h} geometry $[\tau_\alpha^2 \ll (\delta/2t_\alpha)^2]$, where a negative force constant results for $2t_\alpha^2/\delta > K_\alpha$.

The minimization of E_- [eq 5b] with respect to τ_α and τ_r leads to the general defining energy expression (8a).

$$\begin{aligned} &E_-^m = E_{rf}^m - (1/2)(E_{FC}^m - \delta), \text{ with} \\ &E_{rf}^m \equiv (1/2)(E_g^m + E_e^m - \delta) \\ &E_{FC}^m = [(\delta E_{g,e}^m)^2 + 4(N^m)^2]^{1/2} \end{aligned} \tag{8a}$$

Here, E_{rf}^m stands for the energy connected with the restoring force and will be defined below. In the case that $(\delta E_{g,e}^m/2)^2$ is vanishingly small compared to $(N^m)^2$ in [eq 5b], and we will see that this condition is satisfied for nearly all considered molecules at the C_{3v} minima of the ground-state potential surface with not only large α_2'' (τ_α^m) but also α_1' (τ_r^m) nuclear displacements, simple solutions result, implying the following energies and geometrical parameters:

$$\begin{aligned} &(\delta E_{g,e}^m/2)^2 \ll (N^m)^2 \\ &\quad \tau_\alpha^m \cong \beta t_\alpha/K_\alpha \text{ (with } \beta \equiv K_\alpha/K_\alpha^r \text{ and } K_\alpha^r = K_\alpha - t_{\alpha r}^2/K_r) \\ &\quad \tau_r^m \cong (t_{\alpha r}/K_r)\,\tau_\alpha^m \\ &\quad (1/2)E_{FC}^m \cong N^m \cong \beta t_\alpha \tau_\alpha^m \end{aligned} \tag{8b}$$

With the even more restrictive condition $|\delta E_{g,e}^m|/2 \ll N^m$, the relations (8c) would be additionally valid.

$$\begin{aligned} |\delta E_{g,e}^m|/2 \ll N^m \quad & E_-^m \approx -(1/2)t_\alpha\tau_\alpha^m \\ & E_{rf}^m \approx (1/2)t_\alpha\tau_\alpha^m\,(2\beta - 1) \end{aligned} \tag{8c}$$

The equations 8b,c closely resemble those of eq 3, derived without taking the radial parameter τ_r into account ($\tau_r = 0$) and with the same simplification, the factor β allowing for the R-dependence. Figures 5 and 6 define the notations used in eqs 5 and 8, such as E_g, E_e, $\delta E_{g,e}$, E_-, E_+, E_{FC}, δ, δ^o, E_{rf}, τ_r^o, τ_r, and τ_α, the superscript (m) denoting the values at the DFT optimized C_{3v} geometries.

The energy diagram in Figure 6 illustrates the various steps of the vibronic coupling approach according to eq 8a. The transition from D_{3h} to C_{3v}^+ implies the energy alterations without taking the nondiagonal term due to the vibronic interaction between $A_1(A_1')$ and $A_1(A_2'')$ into account ($N^m = 0$). The restoring force energy E_{rf}^m is the shift of the center-of-gravity of the A_1' and A_2'' terms in D_{3h} to that of the two A_1 states in C_{3v} and represents the energy contribution to the total $D_{3h}\rightarrow C_{3v}$ stabilization energy, which is caused exclusively by the nuclear motions (the nonvibronic part of the interaction).

We now face a situation where we have four unknown parameters, t_α, $t_{\alpha r}$, K_α, K_α', while there is the same number of energetic and geometrical parameters available from the DFT calculations, namely $E_-^m = \delta E_t$, E_{FC}^m, τ_r^m, τ_α^m [eqs 5, 8]. The force constants K_r, K_r' (and hence also the radial factor β) as well as the energy difference δ between the $A_2''(E_e)$ and $A_1'(E_g)$ potential curves at $\tau_r = 0$ can be determined separately by DFT.

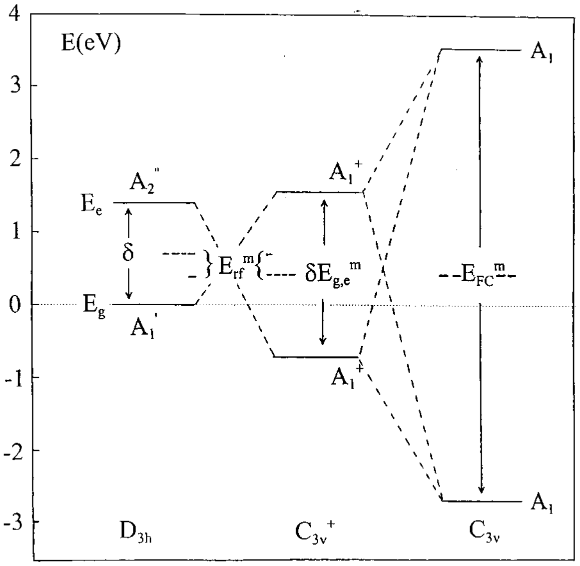

Figure 6. Energy diagram illustrating the steps underlying the vibronic process (see text). C_{3v}^+ shows the state energies without taking the nondiagonal element N^m into account. The numerical values are those of BiH_3; here E_{rf}^m and $\delta E_{g,e}^m$ are of negative sign.

Subsequently, we will analyze more closely how the DFT energies δE_P, δE_{el}, δE_{orb}, $\delta E_{orb}(a_1)$, $\delta E_{orb}(e)$ are related to δ, $\delta E_{g,e}^m$, E_{FC}^m, E_{rf}^m stemming from the vibronic model [eq 8b]. Inspecting eqs 5, 8 and Figures 5, 6, we note that the quantities δ, $\delta E_{g,e}^m$, E_{FC}^m, and hence N^m as well, correspond to vertical Franck−Condon energies without a change in the geometry of the considered molecule, whereas E_{rf}^m accounts for the energy changes caused by nuclear displacements. In contrast, *each* of the DFT energies reflects the geometry change from planar to pyramidal. However, our DFT calculations show that the mentioned vertical energies depend exclusively on δE_{orb}, this meaning that E_{rf}^m comprises the complete electrostatic (δE_{el}) and exchange repulsion (δE_P) contributions to the total energy change δE_t (Tables 1, 3) as well as part of δE_{orb}. The nondiagonal element N^m equals that part of $\delta E_{orb}(a_1)$ which solely reflects the stabilization by the vibronic coupling [eq 9].

$$N^m = \delta E_{orb}^{vib}(a_1) \tag{9}$$

Its magnitude is *independent of the chosen reference* (atomic or ionic fragments). Thus, $\delta E_{orb}(a_1)$ comprises N^m, but strongly contributes particularly to E_{rf}^m also. Choosing $BiCl_3$ as an example (Table 3), where $N^m \cong E_{FC}^m$ ($\delta E_{g,e}^m \cong 0$), one finds that $\delta E_{orb}(a_1)$ participates in E_{rf}^m, N^m, and $\delta/2$ with −2.88, −2.30, and +1.00 eV, respectively. We further note that $\delta E_{orb}^{vib}(a_1)$ is predominantly of angular origin, the radial participation being rather small ($1.0 \le \beta \le 1.1$, see Table 6). $\delta E_{orb}(e)$ is nearly completely part of E_{rf}^m. We conclude that the relations between the energy expressions of the vibronic model and the DFT energies are rather complex, the equality (eq 9) forming the invariant bridge.

The calculated energies N^m and $E_{FC}^m/2$ in Table 5 are, with the exceptions PBr_3, NCl_3, NBr_3, and in particular NH_3− in the latter case the A_1'−A_2'' separation energy δ is the largest of all investigated molecules − mostly identical or deviate from each other by less than 10%. This indicates only small values of $(1/4)(\delta E_{g,e}^m)^2$ in comparison to $(N^m)^2$ and signals close

TABLE 5: Vibronic Coupling (N^m, $(\beta t_\alpha)^2/K_\alpha$) and Franck−Condon ($E_{FC}^m/2$) Energies for Molecules AX_3 in the C_{3v} Geometry (in eV), as Defined in the Text[a]

		H	F	Cl	Br	I
N	N^m	2.39	3.53	1.22	0.81	
	$E_{FC}^m/2$	3.71	3.83	1.42	1.07	0.76
	$(\beta t_\alpha)^2/K_\alpha$	4.67	4.05	1.07	0.82	
	$\eta_{C3v}(\eta_{D3h})$	6.35(6.01)	8.31(5.26)	4.53(3.79)	3.85(3.11)	3.14(2.55)
	$\chi_{C3v}(\chi_{D3h})$	5.32(4.66)	5.72(5.22)	6.00(5.03)	6.00(5.26)	5.72(5.60)
P	N^m	3.59	4.49	2.22	1.34	1.21
	$E_{FC}^m/2$	3.60	4.53	2.40	1.50	1.31
	$(\beta t_\alpha)^2/K_\alpha$	3.71	4.36	1.89	1.49	1.18
	$\eta_{C3v}(\eta_{D3h})$	5.74(4.95)	7.69(4.71)	5.27(3.31)	4.50(2.99)	3.74(2.61)
	$\chi_{C3v}(\chi_{D3h})$	5.19(3.85)	5.17(6.45)	5.17(6.18)	5.26(5.98)	5.23(5.69)
As	N^m	3.47	4.13	2.29	1.86	1.28
	$E_{FC}^m/2$	3.47	4.13	2.32	1.89	1.31
	$(\beta t_\alpha)^2/K_\alpha$	3.50	3.96	2.13	1.76	1.22
	$\eta_{C3v}(\eta_{D3h})$	5.80(4.65)	7.56(4.74)	5.11(3.45)	4.40(3.12)	3.71(2.72)
	$\chi_{C3v}(\chi_{D3h})$	4.99(3.79)	5.44(6.84)	5.50(6.42)	5.47(6.15)	5.36(5.84)
Sb	N^m	3.08	3.60	2.49	2.08	1.45
	$E_{FC}^m/2$	3.23	3.64	2.50	2.08	1.45
	$(\beta t_\alpha)^2/K_\alpha$	2.90	4.29	2.38	1.99	1.41
	$\eta_{C3v}(\eta_{D3h})$	5.31(4.21)	6.83(4.38)	5.01(3.39)	4.39(3.08)	3.65(2.70)
	$\chi_{C3v}(\chi_{D3h})$	4.70(3.74)	5.57(6.57)	5.42(6.37)	5.32(6.08)	5.41(5.93)
Bi	N^m	2.90	3.37	2.29	1.96	1.39
	$E_{FC}^m/2$	3.12	3.41	2.30	1.96	1.39
	$(\beta t_\alpha)^2/K_\alpha$	3.20	3.44	2.30	1.98	1.32
	$\eta_{C3v}(\eta_{D3h})$	5.52(3.50)	6.46(4.67)	4.83(3.56)	4.30(3.24)	3.64(2.84)
	$\chi_{C3v}(\chi_{D3h})$	4.84(4.10)	6.10(7.07)	5.83(6.60)	5.56(6.26)	5.54(6.06)

[a] The molecular hardness η and the electronegativity χ (in eV), for the C_{3v} and D_{3h} symmetry, as derived from DFT calculations, are also listed. η and χ values for the following initial atomic fragments are: $\eta(\chi)$; H: 5.43(7.10); F:7.83(11.89); Cl:5.04(8.87); Br:4.47(8.15); I:3.85(7.31) and N: 6.06(7.67); P:3.93(5.82); As:3.71(5.50); Sb:3.27(5.07); Bi:3.18(4.88).

agreement with eq 8b. The comparison of N^m with the listed total energies $|\delta E_t|$ in Tables 1 and 3 shows that the latter quantity is mostly much smaller than the former one. This implies that the sum of δE_P, which reflects approximately the steric repulsion contribution due to the angular and radial changes along the $(\alpha_2'' + \alpha_1')$ pathway, of δE_{el}, and of the orbital $[\delta E_{orb} - \delta E_{orb}^{vib}(a_1)]$ energy, the latter resulting from the electronic rearrangements during the $D_{3h}\rightarrow C_{3v}$ transition solely without the vibronic energy [eq 9], are nearly always positive. Only in the cases of NBr_3 and PBr_3 is this sum, which corresponds to $(E_{rf}^m + \delta/2)$ [eq 8a], slightly negative, with −0.3 and −0.1 eV respectively, thus supporting the vibronic stabilization effect. *We note as an important conclusion, that the vibronic interaction is the energetically deciding quantity for the symmetry break from D_{3h} to C_{3v}.* We further find that for most of the molecules with $A_1'(a_1')^2$ ground states, the major contribution to N^m stems from the lone pair stabilization $2\delta E_{\alpha 1'}$ due to the vibronic HOMO−LUMO interaction. In the case of the molecules with $A_1'(a_2''^2)$ ground states (exception NH_3), the lone pair stabilization energy $2\delta E_{\alpha 2''}$ is even much larger than N^m (see Tables 1 and 3).

Figure 7 shows a plot of $|E_-^m - \delta/2|$ versus $(1/2)E_{FC}^m(\cong N^m)$. Here the deviations from the straight line perpendicular to the $|E_-^m - \delta/2|$ axis indicate the magnitude of the restoring force contribution E_{rf}^m according to eq 8a. They are positive in most cases and rather small ($|E_{rf}^m| \leq 0.4$ eV), but adopt particularly large positive values for the fluorides with $A_1'(a_1')^2$ ground states (see section IV.2).

We have considered in our vibronic approach only the interaction between the A_1' ground state with the first excited A_2'' state, without including further excited states of A_2'' symmetry. However, because the DFT energies comprise all possible interactions, the calculated coupling and force constants have to be considered as effective parameters, which represent in a not always obvious way all couplings. To gain some insight as to how significant the influence of higher excited states is, separate calculations were performed in the neighborhood of the D_{3h} stationary points, where the condition $N^2 \ll (\delta E_{g,e}/2)^2$ is satisfied; here eq 7b is approximately valid and can be applied in the form of eq 7c,[10b] where a summation over the interaction with n excited A_2'' states occurs.

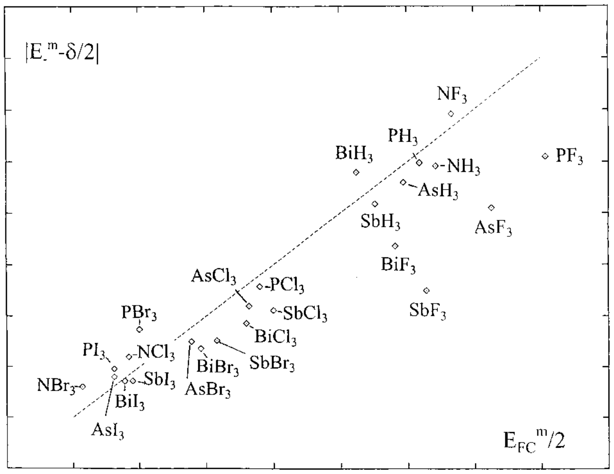

Figure 7. Energy plot of $|E_-^m - \delta/2|$ versus $(1/2)E_{FC}^m$ according to eq 8a. The straight line indicates vanishing E_{rf}^m values, whereas marks above and below the line point to E_{rf}^m energies <0 and >0, respectively.

$$K_\alpha^{tot} \equiv K_\alpha + \Delta K_\alpha^{vib} \cong K_\alpha - 2\Sigma_{(i)} t_{\alpha(i)}'^{2}/\delta_{(i)} \quad (i = 1-n) \qquad (7c)$$

As is outlined in the appendix, in most cases the contribution from the coupling of the A_1' ground state with the lowest excited state A_2'' [$i = 1$] dominates by far the magnitude of ΔK_α^{vib} with at least 75%, approaching 100% in the case of the hydrides where only one excited A_2'' state is available. Exceptions are PF_3 and NF_3 with 66% and 54%, respectively, the extreme being NCl_3 with only 27%. In the latter case the second possible interaction contributes 73%; due to a much larger coupling constant $t_{\alpha(2)}'$, the influence of the also large $\delta_{(2)}$ separation energy is overcompensated. Keeping these exceptions in mind, we may well consider the effective vibronic coupling and force constants, calculated in the two-state vibronic model (Table 5), as representative parameters for the description and parametrization of the $D_{3h}\rightarrow C_{3v}$ symmetry change. We further note that the coupling constants in eq 7c are different from those (t_α) used throughout this contribution (see appendix).

2. The Parametrization and Interpretation of the Vibronic Coupling Effect. According to the described procedure, we have calculated the force constants K_r, K_r' and K_α, K_α' as well as the vibronic coupling constants t_α and $t_{\alpha r}$ by *exactly* solving the system of nonlinear equations for τ_α^m, τ_r^m, E_-^m, and E_{FC}^m, resulting from eqs 5. We may regard βt_α (see the approximate expression for N^m in eq 8b) as the vibronic coupling constant, which represents the angular (t_α) *and* the radial (by the factor β) driving potential for the $D_{3h}\rightarrow C_{3v}$ transition. However, as has been discussed above in detail, this coupling constant images only that part of the process dealing with the orbital interaction between the a_1' and a_2'' MOs, which is induced by the symmetry break, leaving aside all other involved electronic energies. In Table 5 we have listed the stabilization energies $(\beta t_\alpha)^2/K_\alpha$, which should equal N^m and $(1/2)E_{FC}^m$ in the case of very small values for $\delta E_{g,e}^m$ [eq 8b]. Indeed, these values mostly agree with each

TABLE 6: Effective Vibronic Coupling Constants (βt_α, in eV/Å), Vibronic Enhancement Factors Due to $D_{3h}\rightarrow C_{3v}$ A−X Bond Length Changes (β), Angular Force Field Parameters (K_α in eV/Å^2), and Angular Nuclear Displacement Factors τ_α^{m} (corresponding $\beta t_\alpha/K_\alpha$ values resulting from the vibronic model [eq 8b] are also listed) from DFT

		H	F	Cl	Br	I
N	$\beta t_\alpha(\beta)$	3.49(1.04)	3.5(1.0)[a]	1.0(1.0)[a]	0.6(1.05)[a]	
	K_α	2.61	3.0[a]	0.9[a]	0.4[a]	
	$\tau_\alpha^{m}(\beta t_\alpha/K_\alpha)$	0.70(1.34)	1.08(1.15)[a]	1.13(1.1)[a]	1.19(1.4)[a]	≈0.5[b]
P	$\beta t_\alpha(\beta)$	2.55(1.00)	2.83(1.08)	1.09(1.13)	0.68(1.11)	0.63(1.05)
	K_α	1.75	1.84	0.63	0.31	0.34
	$\tau_\alpha^{m}(\beta t_\alpha/K_\alpha)$	1.42(1.46)	1.55(1.54)	1.81(1.73)	1.88(2.18)	1.85(1.87)
As	$\beta t_\alpha(\beta)$	2.25(1.00)	2.36(1.09)	1.15(1.07)	0.89(1.05)	0.65(1.04)
	K_α	1.44	1.40	0.62	0.45	0.35
	$\tau_\alpha^{m}(\beta t_\alpha/K_\alpha)$	1.55(1.56)	1.72(1.68)	1.92(1.85)	2.04(1.98)	1.92(1.86)
Sb	$\beta t_\alpha(\beta)$	1.88(1.00)	1.89(1.06)	1.05(1.06)	0.85(1.05)	0.60(1.02)
	K_α	1.08	0.99	0.47	0.36	0.26
	$\tau_\alpha^{m}(\beta t_\alpha/K_\alpha)$	1.74(1.74)	1.88(1.91)	2.31(2.26)	2.40(2.35)	2.38(2.34)
Bi	$\beta t_\alpha(\beta)$	1.52(1.00)	1.64(1.07)	0.99(1.06)	0.81(1.05)	0.58(1.00)
	K_α	0.73	0.79	0.42	0.33	0.26
	$\tau_\alpha^{m}(\beta t_\alpha/K_\alpha)$	1.95(2.10)	2.04(2.09)	2.30(2.33)	2.41(2.45)	2.32(2.27)

[a] Approximate values, because the two-state model is not valid here. [b] Very approximate value − $A_2''(a_1'^1a_2''^1)$ ground state with close-lying HOMO and LUMO.

other quite satisfactorily. The most striking exception is NH_3, for which molecule a vibronic coupling energy (2.4 eV) is derived being only half of that in magnitude (4.7 eV), which would be expected in the case of small δ (and $\delta E_{g,e}^{m}$) separation energies (Table 1). The vibronic coupling parameter βt_α and ground-state force contant K_α calculated for this molecule (Table 6) are in reasonable agreement with the results of an ab initio calculation.[25]

We will show now that the Franck−Condon energies $(1/2)E_{FC}^{m}$ (equaling in most cases the vibronic coupling energy $N^{m} \cong (\beta t_\alpha)^2/K_\alpha$) and $\delta/2$ are correlated with the hardness $\eta(C_{3v})$ and $\eta(D_{3h})$ of the molecules, respectively. The hardness is defined as the difference between the ionization energy (I) and the electron affinity (A) according to eq 4c and available from the DFT calculations. The indicated correlation should hold, because the energy difference $I - A$ roughly images the transition energy $A_1(A_1')\leftrightarrow A_1(A_2'')$ or $A_1'\leftrightarrow A_2''$, when exciting an electron from the HOMO to the LUMO [eq 10a].

$$\eta(C_{3v}) \cong (1/2)E_{FC}^{m} + C(C_{3v}),\quad \eta(D_{3h}) \cong \delta/2 + C(D_{3h}),$$
$$\text{with } C = (1/2)\,(J_{HL} - 2K_{HL}) \qquad (10a)$$

$$\delta\eta = \eta(C_{3v}) - \eta(D_{3h}) = (1/2)(E_{FC}^{m} - \delta) + \delta C \qquad (10b)$$

The quantities $\eta(C_{3v})$ and $E_{FC}/2$ as well as $\eta(D_{3h})$ and $\delta/2$ differ in an additional interelectronic repulsion contribution C, which results when adding an electron to the LUMO (A) and removing it from the HOMO (I) instead of regarding the real excitation process.[29] The term C is related to U [eq 4b]; J_{HL} and K_{HL} are the Coulomb and exchange integral respectively, whose difference should not vary too much in the series of investigated molecules. This can indeed be deduced from Figure 8a, where the interrelation between $\eta(C_{3v})$ and $E_{FC}^{m}/2$ [or N^{m} or $(\beta t_\alpha)^2/K_\alpha$] is indeed transparent. The gradient of the best-fit straight line in the figure is very near to 1.0, which would be the expected slope for constant C values in dependence on the kind of AX_3 molecule. If the hardness difference $\delta\eta$ is plotted versus $(1/2)(E_{FC}^{m} - \delta)$ [eq 10b], the energy contributions from interelectronic repulsion $C(C_{3v})$ and $C(D_{3h})$ should largely cancel. Figure 8b indeed illustrates that the remaining repulsion term δC is small in most cases (≤ 0.15 eV), approaching 0.5 eV only for three out of 25 molecules.

We deduce from Table 5 and Figure 8a that the quantities $E_{FC}^{m}/2 \cong N^{m} \cong (\beta t_\alpha)^2/K_\alpha$ *and* $\eta(C_{3v})$ *vary according to the*

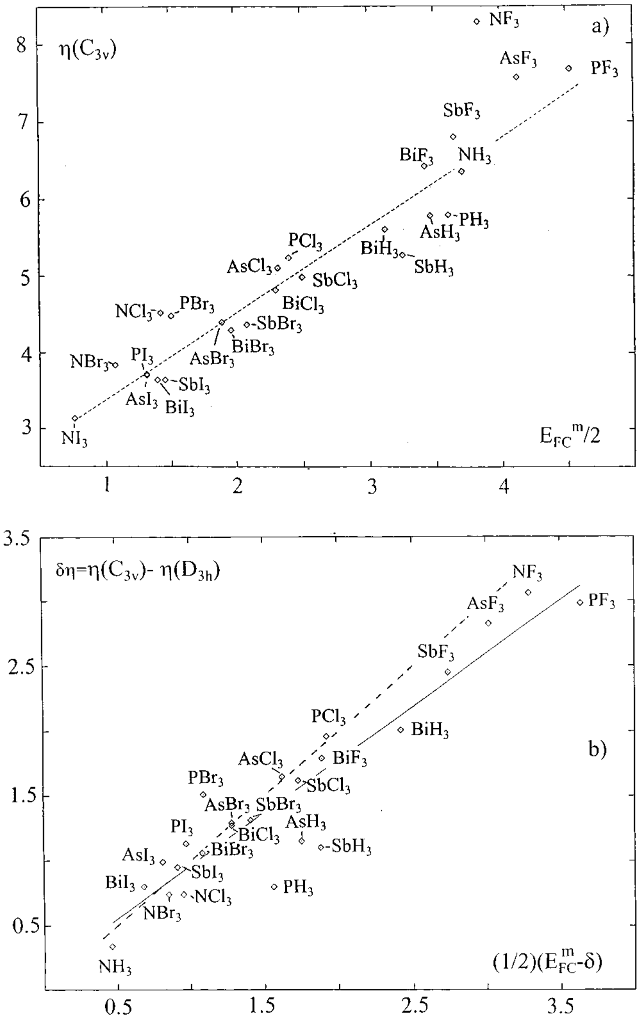

Figure 8. (a) Energy plot of the hardness $\eta(C_{3v})$ versus $(1/2)E_{FC}^{m}$ for AX_3 molecules, from DFT calculations in their C_{3v} ground state geometries. The straight line is a least-squares fit, excluding the NX_3 molecules, according to $\eta_{C3v} = 2.14 + 1.17\,E_{FC}^{m}/2$. (b) Plot of the hardness difference $\delta\eta = \eta(C_{3v}) - \eta(D_{3h})$ versus the transition energy difference in $C_{3v}[A_1(A_2'')\rightarrow A_1(A_1')]$ and $D_{3h}(A_2''\rightarrow A_1')$ $\Delta E = (1/2)(E_{FC}^{m} - \delta)$. The best fit line obeys the equation $\delta\eta = 0.15 + 0.82\,\Delta E$, and the hatched line indicates the equality of $\delta\eta$ and ΔE for vanishing interelectronic repulsion contributions δC [eq 10b].

following sequence of X atoms (with a deviation in the NH_3 case):

$$AX_3{:}\ F > H \gg Cl > Br > I\ (A{:}N,P,As,Sb,Bi) \qquad (11)$$

$$N > P > As > Sb > Bi\ (X{:}H,F) \qquad (11a)$$

The trend (11) is the same for each A atom, though the gradation gets smaller proceeding from N via P to As, Sb, Bi. The dependence on A is only small (for X=H,F) (11a) or not present. Both series also reflect how the atomic hardness (Table 5) varies with X.

The hardness values for the D_{3h} molecular geometry (Table 5) are always smaller than $\eta(C_{3v})$. This observation is closely related to what was originally claimed to be a general principle, first formulated by Pearson[30] and later illustrated by Datta for NH_3.[31] It states that the hardness is minimum at the transition state (here the planar geometry) and reaches the maximum at the energy minimum of the potential curve (C_{3v} geometry; see Figure 5b), on condition that the chemical potential μ does not change during the process. It has been shown though, that the given proof[32] is in error.[33] Our own results indeed do not give any indication that the maximum hardness principle is valid in the cited form, and we will discuss this item in some detail below. However, one *always* observes an *increase* of η, when proceding from the D_{3h} to the optimized C_{3v} geometry (see Figure 10). The reason is obvious, because a stabilization of the A_1' ground state and a destabilization of the excited A_2'' states occurs via the vibronic coupling, thus enhancing the Franck−Condon energy from δ to E_{FC}^m and $\eta(D_{3h})$ to $\eta(C_{3v})$ [eq 10b]. Again this mostly considerable energy effect is only small for NH_3 because of the large initial δ value.

The correlation between the vibronic coupling energy and the total energy change during the $D_{3h}\rightarrow C_{3v}$ transition is rather complex. The equality of $|\delta E_t| = |E_-^m|$ with $(1/2)\beta t_\alpha^2/K_\alpha$, suggested by eq 8c, does not hold for the larger part of the AX_3 molecules, because the more severe critical condition $|\delta E_{g,e}^m|/2 \ll N^m$ is not met in these cases. The largest deviations from the simple relationship are observed for NH_3 and NF_3, where the energies $|E_{g,e}^m|/2$ (N^m) adopt values of 2.8 (2.4) and 1.5 (3.5) eV, respectively. In difference, E_{FC}^m approximately equals N^m and $(\beta t_\alpha)^2/K_\alpha$, as considered above [Table 5, eq 8b].

In what follows, we derive relations between the changes of η and of the chemical potential μ during the $D_{3h}\rightarrow C_{3v}$ transition and quantities such as δE_t^m, E_{FC}^m, δ, and E_{rf}^m. Going back to the definitions of μ (or the electronegativity χ) and the hardness [eq 4c], we readily obtain eq 12a with a useful correlation between η, μ, and the total energy E_t^m.

$$\eta - \mu = I = E_t^m(+1) - E_t^m \quad \text{or} \qquad (12a)$$

$$E_t^m = E_t^m(+1) + \mu - \eta \Rightarrow \delta E_t^m = \delta E_t^m(+1) + \delta\mu - \delta\eta$$

Here $E_t^m(+1)$ and $\delta E_t^m(+1)$ denote the total energy of the singly ionized molecules $(AX_3)^+$ and its change during the $D_{3h}\rightarrow C_{3v}$ transition, calculated for the unrelaxed geometries with respect to $(AX_3)^o$. We may then compare the expression for δE_t^m with that obtained earlier, $\delta E_t^m = E_{rf}^m - (1/2)(E_{FC}^m - \delta)$ [eq 8a]. Having in mind that $\delta\eta$ approximately equals $(1/2)(E_{FC}^m - \delta)$ [eq 10b], one deduces eq 12b, δC being a rather small quantity.

$$\delta E_t^m = E_{rf}^m - \delta\eta + \delta C = E_{rf}^{m'} - \delta\eta$$

$$E_{rf}^{m'} = \delta\mu + \delta E_t^m(+1) \qquad (12b)$$

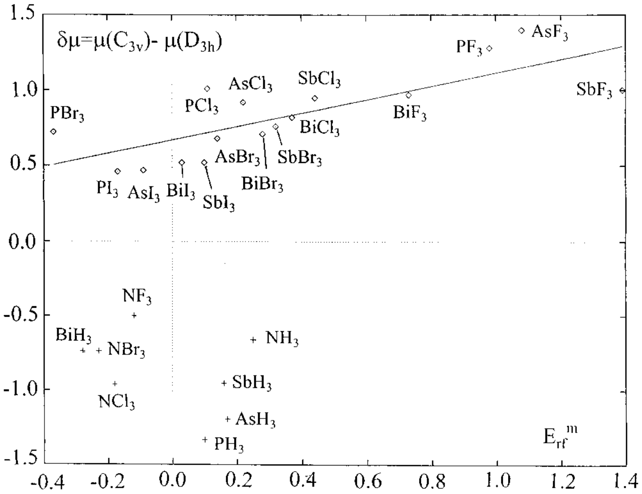

Figure 9. Energy plot of $\delta\mu = \mu(C_{3v}) - \mu(D_{3h})$ versus E_{rf}^m, with "s²" and "p²" type AX_3 compounds appearing in different segments of the figure (see text).

We conclude that the hardness principle is obviously restricted by certain properties of E_{rf} rather than of μ, at least if vibronically induced symmetry changes of molecules or structural fragments are considered. Explicitly, the hardness can only be maximal at the minimum E_-^m if the relation $(dE_{rf}'/dP) = 0$ at P_m holds, where P_m is the distortion coordinate due to the angular (θ) and radial (R) $D_{3h}\rightarrow C_{3v}$ changes [eqs 6] at the energy minimum $\delta E_t = E_-^m$.

$E_{rf}^{m'}$ is imaged by $\delta\mu$ only vaguely, because $\delta E_t^m(+1)$ is of comparable magnitude. The latter energy is positive for $A_1'(a_2''\,2)$ ground states and opposes $\delta\mu$ (<0), which supports the vibronic stabilization in these cases (Table 5). A reverse situation arises for $A_1'(a_1'2)$ ground states [$\delta\mu > 0$; $\delta E_t^m(+1) < 0$]. Accordingly the $\delta\mu$ versus E_{rf}^m plot, which we show in Figure 9, discriminates between the two alternative ground states. While a reasonable correlation exists for the "s²" type molecules in the upper part of the figure, with $\delta E_t^m(+1)$ contributions as negative as ≈ -1 eV, the "p²" type compounds appear in the lower left segment, with $\delta E_t^m(+1)$ approaching values up to 0.8 eV. For the molecules studied in this contribution, E_{rf}^m [eq 12b] adopts energies between about 1.4 and −0.4 eV, whereas $\delta\eta$ possesses values in the range between 0.4 and 3.1 eV (Table 5). Correspondingly, a behavior more complex than predicted by the hardness principle is expected. Indeed, if one plots $\delta\eta$ versus $\delta\theta$ (with an optimization with respect to R for each point as well), maximum hardness is either achieved at $\theta > \theta_m$ or $\delta\eta$ has no maximum at all. This can be taken from Figure10a,b which shows the angular variation of δE_t, $\delta\eta$, $\delta\mu$, and $E_{rf}^{m'}$ for PH_3 and SbF_3. The dependencies for the former molecule are characteristic for $A_1'(a_2''^2)$ D_{3h} ground states, with an approximately parabolic increase of $\delta\eta$ and a similar but even more pronounced increase of $E_{rf}^{m'}$ after a minimum at $\theta < \theta_m$. For molecules with an $A_1'(a_1'^2)$ ground state in D_{3h}, maximum hardness $\delta\eta$ might be achieved at $\theta > \theta_m$. In the case of SbF_3, for example, $\delta\eta$ reaches the extremum value at $\theta \cong \theta_m$+4°; here E_{rf}' possesses an inflection point with a rather small gradient, which compensates the gradient of δE_t at the same angle eq [12b]. $\delta\mu$ is maximal at θ_m, without, however, leading to an extremum of $\delta\eta$ at this angle, as demanded by the old version of the hardness principle. Figure 10c depicts the situation for NH_3 with a large initial splitting δ (Table 1). Nevertheless $\delta\eta$, imaging the vibronic energy gain, increases in a comparably pronounced way with $\delta\theta$ as for PH_3, but the restoring force E_{rf}' opposes this tendency very

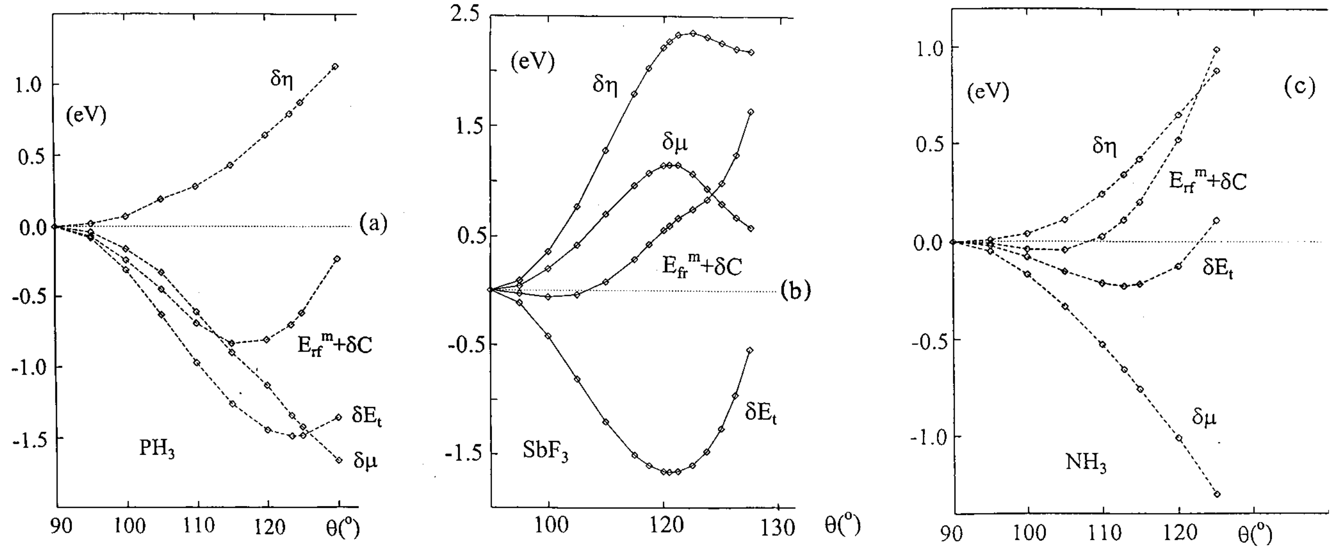

Figure 10. The dependence of δE_t, $\delta\eta$, $\delta\mu$, and $E_{rf}' = E_{rf} + \delta C = \delta\mu + \delta E_t(+1)$ on the angular distortion θ [eq 6b] for PH_3 (a), SbF_3 (b), and NH_3 (c), as obtained from DFT calculations. For each point, an optimization with respect to the radial parameter R has been performed.

efficiently, shifting the energy minimum δE_t^m to rather small distortion angles. Our calculations do not give any indication for a maximum of $\delta\eta$ at $\delta\theta_m$, as has been claimed previously.[31]

We proceed by checking on which molecular properties the variation of the vibronic coupling constant βt_α (Table 6) with the kind of A and X atoms depends, and we readily find that the relations of eqs 11 and 11a, which are valid for the vibronic coupling energy $(\beta t_\alpha)^2/K_\alpha$ (Table 5), hold also here. The factor β, which accounts for the vibronic effect of the radial changes due to the term $t_{\alpha r}\tau_r^m$ [see eqs 5b and 8b)], is generally larger than or equal to unity (exception: NF_3) and indicates that the vibronic interaction energy is enhanced by the radial effect. The latter is small, however, with β possessing values around 1.00 for the hydrides and up to only 1.1 for the halides; the extreme example is PCl_3, where the radial compression enhances the angular vibronic force by 13% (Table 6). We note here, that the effective vibronic coupling constant βt_α is a quantity that comprises different contributions due to A−X, A−A, and X−X interactions. Controversial opinions, as to which interaction is the most significant (A−A, purely ionic[34,35] or A−X, covalent[36]) occur in the literature. An analysis of the orbital vibronic constant t_α^{orb} pertaining to the HOMO−LUMO vibronic mixing indicates (see appendix) that this parameter is dominated by A−X overlap terms, contributions due to A−A and X−X terms being much smaller and negligible, respectively.

It is surpising at first sight that τ_α^m, as obtained from the DFT calculations and equivalent to the bond angles α in Tables 1 and 3, displays a distinctly different dependence on A and X than the vibronic coupling constant βt_α. Explicitly, one observes the following trend for the extent of distortion (Table 6) when changing the ligand according to

$$\tau_\alpha^m\text{: } H < F < Cl \lesssim Br \approx I \text{ [A:N to Bi]} \qquad (13)$$

and the metal according to

$$\tau_\alpha^m\text{: } N \ll P < As < Sb \le Bi \text{ [X:H,F to I]} \qquad (13a)$$

We have listed the $\beta t_\alpha/K_\alpha$ values, which should equal τ_α^m in the case of small or vanishing $(1/2)\delta E_{g,e}^m$ energies [eq 8b], in Table 6 as well. They are generally in good agreement with τ_α^m, with the exceptions of PBr_3 and in particular NH_3. The reason for the deviating trends (eqs 13 and 13a) from those for βt_α (eqs 11 and 11a), which are approximately opposite, is obviously the influence of the force constant K_α, which controls τ_α^m besides the vibronic coupling constant βt_α. As one easily deduces from Table 6, K_α equally follows the dependencies (eqs 11 and 11a) except for hydrogen, but decreases more steeply from H ≈ F to Cl, Br, I, and from N to Sb than βt_α does. Hence the largest angular distortions result for Sb(Bi)Br_3 with $\tau_\alpha^m \cong$ 2.4 Å (α ≅ 98°) and the smallest ones for NH_3 (strongly reduced in addition by a large initial splitting δ) and NF_3 with $\tau_\alpha^m \cong$ 0.7 Å (α ≅ 106°) and $\tau_\alpha^m \cong$ 1.1 Å (α ≅ 102°), respectively. We conclude that the observable quantity τ_α^m, which measures the angular distortion of an AX_3 molecule, is largest for entities with "soft" constituents of low hardness values, such as Bi^{III}, Sb^{III} and I^-, Br^-, while small τ_α^m values are characteristic for the "harder" molecules. The vibronic coupling energy $N^m \cong (\beta t_\alpha)^2/K_\alpha$ is less influenced by K_α than τ_α^m and still follows the sequences of eqs 11 and 11a as discussed before, with a less distinct gradation, however. We emphasize that the relations of eqs 13 and 13a may not necessarily hold for other coordination numbers (subject of a subsequent study), because they depend critically on the force constants of the AX_3 molecules. Thus, it is doubtful at present, whether these relations (eqs 13 and 13a) can serve as a general empirical series to predict lone pair induced distortions.

V. Conclusions

Model DFT calculations on "lone pair" molecules AX_3 (A:N to Bi; X:H,F to I) show, in contrast to, for example, TlX_3 compounds, a distinct steric effect, leading to a C_{3v} distortion of the parent D_{3h} geometry along a distortion path according to the $(\alpha_1' + \alpha_2'')$ vibrations. As was demonstrated, the energetic and steric changes can be parametrized successfully by a vibronic coupling approach. The most significant results of this contribution are listed in the following.

(1) An analysis that decomposes the total DFT binding energies into steric, ionic, and orbital interaction terms indicates that the driving force for the $D_{3h} \rightarrow C_{3v}$ transition, consisting of radial (bond length alteration) and angular changes, is dominated by the steric repulsion energy for "p_z^2" type molecules (δE_P), but by orbital stabilization δE_{orb} in the case of molecules with "s^2" type ground states (Tables 1 and 3). The underlying reason

is the distinct change of the A−X spacings during the $D_{3h}\rightarrow C_{3v}$ transition, which increase in the former case due to the ns(A) admixture to the HOMO, thus favoring $\delta E_{\mathrm{P}}(<0)$ and leading to weaker bonds ($\delta E_{\mathrm{orb}} > 0$). The reverse phenomenon occurs for the "s^2" type molecules, where a shrinking of the interatomic distances occurs ($\delta E_{\mathrm{P}} > 0$; $\delta E_{\mathrm{orb}} < 0$).

(2) Separating the various contributions to the DFT energy changes (δE_{t}, δE_{P}, δE_{el} and δE_{orb}) according to bond length and angular alterations, it is found that δE_{P} (as well as δE_{el}) depends nearly exclusively on the radial distortion coordinate. We conclude that the angular distortions induced by the "lone pair" are caused by specific orbital effects rather than by other forces: *Apparently steric interactions or "interpair repulsions," as in the classical VSEPR model, do not play a significant energetic role.*

(3) The HOMO in D_{3h} is of $a_{1g}'^{2}(s^2)$ type in most cases; here the lone pair density is predominantly delocalized toward the ligands (Figures 2 and 2a). In difference, in the cases of the hydrogen compounds and the NX_3 (X=F,Cl,Br) molecules, the HOMO is of $a_2''^{2}(p_z^2)$ nature and predominantly localized on A, but adopts considerable ligand character by the vibronic interaction (Figures 3, 3a and 4; Tables 1 and 3). NI_3 is presumably an intermediate case with an $(a_1'^{1}a_2''^{1})$ HOMO.

(4) The interpretation of the DFT data using a simple vibronic coupling model based on an effective two state approximation [$A_1'(a_1'^2$ or $a_2''^2)$ and $A_2''(a_1'^1a_2''^1)$] yields a rather good description for the considered molecules, except for the nitrogen halogenides; here more remote excited states (NCl_3) and near degeneracy effects of the HOMO and the LUMO (NI_3) are significant. Deduced effective vibronic coupling parameters βt_α (β standing for the radial and t_α for the angular orbital effect) and force constants K_α [eqs 5 and 8 and Tables 5 and 6] allow a parametrization of the observed steric and energetic changes during the $D_{3h}\rightarrow C_{3v}$ transition.

It is obviously the vibronic stabilization [$\approx -(\beta t_\alpha)^2/K_\alpha$] originating mainly from the interacting a_1'(ns) and a_2''(np_z) MOs after the $D_{3h}\rightarrow C_{3v}$ symmetry break according to eqs 8 and 9, with generally $(\beta t_\alpha)^2/K_\alpha \geq |\delta E_t^m|$ (Tables 1, 3 and 5), that governs the total energy gain δE_t^m. The additional energy contributions from the electronic rearrangements in the MOs during the $D_{3h}\rightarrow C_{3v}$ transition overcompensate $-(\beta t_\alpha)^2/K_\alpha$ only in the case of "p_z^2" type molecules, rendering positive δE_{orb} values here (see under 1).

(5) The vibronic energy dominating the $D_{3h}\rightarrow C_{3v}$ transition and represented by $(\beta t_\alpha)^2/K_\alpha$ (Table 5) is strongly correlated with the hardness of the AX_3 molecules (Figures 8a,b). *Its effect is due to the nondiagonal element in matrix (5a) and large for the hard and small for the soft molecules, according to the sequences of eqs 11a and b.* The vibronic coupling constants βt_α themselves follow the same trend in an even more distinct fashion (Table 6).

(6) In contrast, the angular distortion $\tau_\alpha^{\mathrm{m}} \cong \beta t_\alpha/K_\alpha$ (Table 6) as a significant observable quantity for the chemist follows nearly opposite sequences (eqs 13 and 13a) due to the strong influence of K_α, which varies analogously to βt_α in dependence on A and X (eqs 11a,b), but with a more pronounced gradation. The extent of the PJT distortion becomes more pronounced in the here-considered case of AX_3 molecules, the softer the AX_3 molecule and its atomic constituents are.

(7) The total energy gain $\delta E_{\mathrm{t}}^{\mathrm{m}}$ in the course of the $D_{3h}\rightarrow C_{3v}$ transition is the sum of two contributions (Figure 7). The first of these is the "corrected" vibronic coupling energy $(1/2)(E_{\mathrm{FC}}^{\mathrm{m}} - \delta)[E_{\mathrm{FC}}^{\mathrm{m}} \cong (\beta t_\alpha)^2/K_\alpha]$, which approximately equals the hardness difference $\delta\eta = \eta(C_{3v}) - \eta(D_{3h})$ (Figure 8b). The second contribution is $E_{\mathrm{rf}}^{\mathrm{m}}$ and represents the restoring force, which reflects the electronic and nuclear rearrangement energy during the $D_{3h}\rightarrow C_{3v}$ transition without accounting for the vibronic ground state−excited state interaction (Figure 6). *We find (see Figs 10) that the "hardness principle" (maximum hardness at the optimized C_{3v} geometry) is not restricted by a constant chemical potential (μ) during the considered process as previously claimed, but by the condition $(\partial E_{rf}/\partial P)_m \approx 0$ (P: distortion coordinate).*

(8) The exceptional position of NH_3 among the AX_3 molecules, i.e., the unexpectedly small angular distortion and the only tiny $\delta E_{\mathrm{t}}^{\mathrm{m}}$ stabilization energy, is caused mainly by the very large initial $A_1'-A_2''$ energy gap δ (Table 1). The vibronic coupling model would otherwise suggest much larger τ_α^{m} and $|\delta E_{\mathrm{t}}^{\mathrm{m}}|$ values than actually observed (Table 6).

Acknowledgment. The authors are grateful to Prof. Dr. G. Frenking (Fachbereich Chemie, Marburg, Germany) and Dr. F. Cimpoesu (Institute of Physical Chemistry, Bucharest, Romania) for critically reading the manuscript and for valuable discussions. We furthermore thank the Deutsche Forschungsgemeinschaft for financial support. This contribution is dedicated to Prof. Dr. U. Müller (Marbürg) on the occasion of his 60th birthday.

Appendix: Derivation of Orbital Vibronic Constants [$t_{\alpha(i)}'$] and Their Analysis

Here we describe a general procedure for calculating vibronic coupling parameters $t_{\alpha(i)}'$ in a one-electron picture [eq 7c] if pairs of orbitals are intermixed by distortions, say from D_{3h} to C_{3v} geometry, via the operator $(\partial h/\tau_\alpha)_o$: $t_{\alpha(i)}' = \langle\varphi(a_1')|(\partial h/\tau_\alpha)_o|\varphi(a_2'')\rangle$. Let us denote the matrices of eigenvectors (in columns), eigenvalues and the overlap, written in the basis of atomic wave functions, by V, Λ (diagonal), and S, respectively. Calculations of higher quality require the use of extended basis sets, approximating a given valence orbital in terms of two or more Slater exponents. Following the general theory of effective Hamiltonians,[37] it is possible to reconstruct from these data a matrix (H_{eff}) in which a single function represents a given valence orbital. Choosing as an example NF_3 and a triple-ζ basis for N and F, the 19 × 19 secular problem can be reduced to a 5 × 5 problem, involving three a_1' [2s(N), 2s(F), and $2p_{x,y}$(F)] and two a_2'' [$2p_z$(N) and $2p_z$(F)] orbital functions. If we denote by V_{S}, Λ_{S}(diagonal), and S_{S} the submatrices of V, Λ, and S, which operate within the restricted valence orbital basis (5 × 5) space, H_{eff} is given by eq A.1 where V^{T} is the transpose of the effective eigenvector matrix V as given in eq A.2. The Löwdin orthogonalization [eq A.3] eliminates overlap due to the nonorthogonality of the atomic basis functions, whereas eq A.4 is the key step which leads to the effective eigenvectors in the restricted orbital subspace, a procedure developed by des Cloizeaux.[38]

$$H_{\mathrm{eff}} = V\Lambda_{\mathrm{S}}V^{\mathrm{T}} \tag{A.1}$$

$$V = S_{\mathrm{L}}^{-1/2}V_{\mathrm{L}} \tag{A.2}$$

$$V_{\mathrm{L}} = S_{\mathrm{S}}^{1/2}V_{\mathrm{S}} \tag{A.3}$$

$$S_{\mathrm{L}} = V_{\mathrm{L}}V_{\mathrm{L}}^{\mathrm{T}} \tag{A.4}$$

In the considered case, namely vibronic coupling inducing a $D_{3h}\rightarrow C_{3v}$ distortion, H_{eff} is calculated for an arbitrary but small distortion angle θ [eq 6b with $\delta\theta = 5°$]. If we denote the respective matrices $H_{\mathrm{eff}}(C_{3v})$ and $H_{\mathrm{eff}}(D_{3h})$, the Hamiltonian ΔH_{eff} of eq A.5 results for the vibronic perturbation. The matrix of the expectation values of ΔH_{eff} within the manifold of the a_1' and a_2'' eigenfunctions $V(D_{3h})$ yields, after division by τ_α, the matrix of $t_{\alpha(i)}'$ orbital vibronic coupling parameters V_{vib} eq A.6, which consists of vanishingly small diagonal and much larger off-diagonal $a_1' - a_2''$ matrix elements.

$$\Delta H_{\mathrm{eff}} = H_{\mathrm{eff}}(C_{3v}) - H_{\mathrm{eff}}(D_{3h}) \tag{A.5}$$

$$V_{\mathrm{vib}} = [V^{\mathrm{T}}(D_{3h})\Delta H_{\mathrm{eff}} V(D_{3h})]/\tau_\alpha \tag{A.6}$$

In calculating $H_{\mathrm{eff}}(D_{3h})$ and $V(D_{3h})$ use has been made of the approximation that for small τ_α values the eigenvector matrix $V(C_{3v})$ differs only slightly from $V(D_{3h})$. The renormalization after setting the small $a_2''(a_1')$ AO coefficients in the $a_1'(a_2'')$ eigenvectors to zero, and vice versa, yields $V(D_{3h})$ and $H_{\mathrm{eff}}(D_{3h})$. Taking again NF_3 as an example, the following values of $t_{\alpha(i)}'$, $\delta_{(i)}$, and of the corresponding contributions $\Delta K_\alpha{}^{\mathrm{vib}}{}_{(i)} = -2t_\alpha{}'_{(i)}{}^2/\delta_{(i)}$ to the total force constant $K_\alpha{}^{\mathrm{tot}}$ [eq 7c] result for the two possible $a_2''-a_1'$ interactions:

	i	$t_{\alpha(i)}'$	$\delta_{(i)}$	$\Delta K_\alpha{}^{\mathrm{vib}}{}_{(i)}$
$1a_2''-3a_1'$(LUMO):	2	3.23	9.42	−2.22
$2a_2''$(HOMO)$-3a_1'$(LUMO):	1	1.01	0.77	−2.66

(A.7)

The larger $\delta_{(2)}$ separation energy between the lower lying $1a_2''$ orbital and the LUMO is nearly compensated by the larger $t_{\alpha(2)}'$ parameter in comparison to the HOMO−LUMO interaction, yielding comparable contributions to $\Delta K_\alpha{}^{\mathrm{vib}}$ from the two terms. The coupling constants $t_{\alpha(i)}'$ cannot be compared directly with t_α [eq 8b] for mainly two reasons: on one hand, t_α is an effective many-electron parameter representing all possible orbital interactions and, on the other hand, t_α is calculated at $\tau_\alpha{}^{\mathrm{m}}$, in contrast to the $t_{\alpha(i)}'$, which are derived at very small τ_α distortions. Calculated values for $\Delta K_\alpha{}^{\mathrm{vib}}$, the sum over all $\Delta K_{\alpha(i)}$ contributions, and for the total force constant $K_\alpha{}^{\mathrm{tot}}$ in D_{3h} (in eV/ Å) according to eq 7c are listed in eq A.8.

A/X		H	F	Cl	I	
N	$\Delta K_\alpha{}^{\mathrm{vib}}$ (%)	−1.49(100)	−4.88(54)	−2.33(26)		(A8)
	$K_\alpha{}^{\mathrm{tot}}$	−0.86	−7.59	−1.81		
P	$\Delta K_\alpha{}^{\mathrm{vib}}$ (%)	−2.24(100)	−4.14(66)	−2.31(74)	−1.38(80)	
	$K_\alpha{}^{\mathrm{tot}}$	−1.63	−2.55	−1.47	−0.71	
As	$\Delta K_\alpha{}^{\mathrm{vib}}$ (%)	−2.16(100)	−3.45(76)	−2.03(82)	−1.21(85)	
	$K_\alpha{}^{\mathrm{tot}}$	−1.87	−1.85	−1.02	−0.50	
Sb	$\Delta K_\alpha{}^{\mathrm{vib}}$ (%)	−1.36(100)	−2.35(75)	−1.40(80)	−0.94(84)	
	$K_\alpha{}^{\mathrm{tot}}$	−3.49	−1.50	−0.92	−0.46	
Bi	$\Delta K_\alpha{}^{\mathrm{vib}}$ (%)	−3.78(100)	−1.95(85)	−1.34(88)	−0.81(89)	
	$K_\alpha{}^{\mathrm{tot}}$	−4.51	−0.90	−0.66	−0.36	

The percentage contribution of the HOMO−LUMO interaction (i=1) to $\Delta K_\alpha{}^{\mathrm{vib}}$ is also given (in parentheses). As stated before, the latter interaction usually dominates $\Delta K_\alpha{}^{\mathrm{vib}}$, the NX_3 molecules (in particular NCl_3) being exceptions.

We may use the HOMO−LUMO vibronic coupling parameter $t_{\alpha(1)}'$ as a probe for analyzing the various contributions from the A−A, A−X, and X−X interactions. Choosing, for example, an $a_1'^2$ ground state, the HOMO (φ_g) and the LUMO (φ_e) are represented by the MOs in eq A.9, with s_A and p_{zA} denoting central atom orbitals and X_g and X_e symmetry adapted linear combinations of ligand orbitals of a_1' and a_2'' symmetry, respectively. The HOMO−LUMO coupling parameter can now be specified as in eq A.10.

$$\varphi_g(a_1') = \beta_g s_A + \gamma_g X_g; \quad \varphi_e(a_2'') = \beta_e\, p_{zA} + \gamma_e\, X_e \tag{A.9}$$

$$\begin{aligned} t_{\alpha(1)}' &\equiv \langle \varphi_g(a_1')\,|(\partial h/\tau_\alpha)_o|\varphi_e(a_2'')\rangle \\ &= t_\alpha'(A-A) + t_\alpha'(A-X) + t_\alpha'(X-X) \\ &= \{\beta_g\beta_e(s_A|(\partial h/\partial\tau_\alpha)_o|p_{zA})\} + \{\beta_g\gamma_e\,(s_A|(\partial h/\partial\tau_\alpha)_o|X_e) + \\ &\qquad \beta_e\gamma_g\,(p_{zA}|(\partial h/\partial\tau_\alpha)_o|X_g)\} + \{\,\gamma_g\gamma_e\,(X_g|(\partial h/\partial\tau_\alpha)_o|X_e)\} \end{aligned} \tag{A.10}$$

Here, the term $t_\alpha'(A-A)$ is of purely electrostatic nature, whereas $t_\alpha'(A-X)$ results from the A−X overlap. $t_\alpha'(X-X)$ is mainly due to ligand−ligand interaction and mostly rather small or vanishing ($\gamma_e = 0$: nonbonding p_{zA} MOs). Calculated values [eq A.11] indicate that $t_{\alpha(1)}'$ is generally dominated by A−X overlap. The electrostatic term $t_\alpha'(A - A)$ is either opposing or supporting the overlap contribution, the absolute value being always distinctly smaller than $t_\alpha'(A - X)$ though. The high covalency, particularly of NH_3 and NF_3, the compounds with the hardest atomic fragments (Table 6), is striking; the also large electrostatic terms apparently stabilize the planar geometry, thus reducing the coupling constant considerably. The rather pronounced $t_\alpha'(X - X)$ contribution of PI_3 seems to indicate stabilizing I − I overlap in C_{3v} favored by the small ionic radii ratio of *P* in comparison to *I*. It is surprising that the t_α values from Table 6 follow the same trend in dependence on the kind of AX_3 molecule as do the $t_\alpha'(A-X)$ coupling constants in the listing (A11).

	NH_3	PH_3	BiH_3	NF_3	PF_3	BiF_3	PI_3	BiI_3	
$t_\alpha'(A-A)$	−1.23	0.27	0.35	−2.00	−0.39	0.18	−0.14	0.02	(A11)
$t_\alpha'(A-X)$	3.17	1.67	0.91	2.91	1.66	1.14	0.61	0.54	
$t_\alpha'(X-X)$				0.11	0.18	0.12	0.47	0.08	
$t_\alpha'{}_{(1)}$	1.94	1.94	1.26	1.01	1.45	1.44	0.94	0.64	
t_α	3.35	2.55	1.52	3.50	2.62	1.53	0.60	0.58	

References and Notes

(1) Sidgwick, N. V.; Powell, H. M. *Proc. R. Soc.* **1940**, *A176*, 153.

(2) (a) Gillespie, R. J.; Nyholm, R. S. *Q. Rev. (London)* **1957**, *11*, 339−380. (b) Gillespie, R. J. *Coord. Chem. Rev.* **2000**, *197*, 51−69.

(3) (a) Lennard-Jones, J. E.; Pople, J. A. *Proc. R. Soc. (London)* **1950**, *A202*, 166. (b) Linnett, J. W.; Poee, A. J. *Trans. Faraday Soc.* **1951**, *47*, 1033−1041. (c) Mellish, C. E.; Linnett, J. W. *ibid.* **1954**, *50*, 657−664, 665−670. (d) Dickens, P. G.; Linnett, J. W.; Phil, D. *Q. Rev. (London)*, **1957**, *11*, 291−312. (e) Linnet, J. W. *Can. J. Chem.* **1958**, *36*, 2430. (f) Fowles, G. W. A. *J. Chem. Educ.* **1957**, *34*, 187.

(4) Bartel, L. S. *J. Chem. Educ.* **1968**, *45*, 754−767 and cited references.

(5) (a) Bader, R. F. W.; Gillespie, R. J.; MacDougall, P. J. *J. Am. Chem. Soc.* **1988**, *110*, 7329−7336. (b) Bader, R. F. W. *Coord. Chem. Rev.* **2000**, *197*, 71−94.

(6) (a) Breidung, J.; Thiel, W. *J. Comput. Chem.* **1992**, *13*, 165−176. (b) Schwerdtfeger, P.; Hunt, P. In *Advances in Molecular Structure Research*; Hargittai, M., Hargittai, I., Eds.; JAI Press: Stamford, Connecticut, 1999; Vol. 5, p 223.

(7) (a) Mattheis, L. F.; Gyorgy, E. M.; Johnson, D. W., Jr. *Phys. Rev. B* **1988**, *37*, 3745. Cava, R. J.; Battlog, B.; Krajewski, J. J.; Farrow, R.; Rupp, L. W., Jr.; White, A. E.; Short, K.; Peck, F. E.; Kometani, T. *Nature* **1988**, *332*, 814. (b) Sleight, A. W.; Gillson, J. L.; Bierstedt, P. E. *Solid State Commun.* **1975**, *17*, 27.

(8) (a) Brown, I. D. *Can. J. Chem.* **1964**, *42*, 2758−2767. (b) Lawton, S. L.; Jacobson, R. A. *Inorg. Chem.* **1966**, *5*, 743−749.

(9) (a) Warda, S. A.; Pietzuch, W.; Massa, W.; Kesper, U.; Reinen, D. *J. Solid State Chem.* **2000**, *149*, 209−217. (b) Berghöfer, G.; Reinen, D.; Akhtar, G.; Hormes, J. *Mod. Phys. Lett. B* **1993**, *7*, 1133−1140.

(10) (a) Öpik, U.; Pryce, M. H. L. *Proc. R. Soc. London, Ser. A* **1957**, *238*, 425. (b) Bader, R. F. W. *Can. J. Chem.* **1962**, *40*, 1164−1175. (c) Pearson, R. G. *J. Am. Chem. Soc.* **1969**, *91*, 4947−4955. For an excellent presentation see (d) Pearson, R. G. *Symmetry Rules for Chemical Reactions, Orbital Topology and Elementary Processes*; John Wiley and Sons: New York, 1976.

(11) (a) Bersuker, I. B. *The Jahn−Teller Effect and Vibronic Interactions in Modern Chemistry*; Plenum Press: New York, 1984; p 61. (b) Bersuker, I. B. *Electronic Structure and Properties of Transition Metal Compounds*; John Wiley and Sons: New York, 1996; Chapter 9. (c) Maaskant, W. J. A.; Bersuker, I. B. *J. Phys.: Condens. Matter* **1991**, *3*, 37−47.

(12) (a) Baerends, E. J.; Ellis, D. E.; Ros, P. *Chem. Phys.* **1973**, *2*, 41−51. (b) Baerends, E. J.; Ros, P. *Chem. Phys.* **1973**, *2*, 52−59.

(13) Baerends, E. J.; Ros, P. *Int. J. Quantum Chem. Symp.* **1978**, *12*, 169−190.

(14) Boerrigter, P. M.; te Velde, G.; Baerends, E. J. *Int. J. Quantum Chem.* **1988**, *33*, 87−113.

(15) te Velde, G.; Baerends, E. J. *J. Comput. Phys.* **1992**, *99*, 84 and references therein.

(16) Vosko, S. H.; Wilk, L.; Nusair, M. *Can. J. Phys.* **1980**, *58*, 1200−1211.

(17) Becke, A. D. *Phys. Rev. A* **1988**, *38*, 3098−3100.

(18) Perdew, J. P. *Phys. Rev. B* **1986**, *33*, 8822−8824.

(19) (a) Baerends, E. J.; Gritsenko, O. V.; van Leeuwen, R. In *Chemical Applications of Density-Functional Theory*; Laird, B. B.; Ross, B. B.; Ziegler, T., Eds.; American Chemical Society: Washington, DC, **1996**, Vol. 629; p 20. (b) Baerends, E. J.; Gritsenko, O. V. *J. Phys. Chem.* **1997**, *101*, 5383−5403.

(20) Stowasser, R.; Hoffmann, R. *J. Am. Chem. Soc.* **1999**, *121*, 3414−3420.

(21) (a) Ziegler, T.; Rauk, A. *Theor. Chim. Acta* **1977**, *46*, 1−10. (b) Ziegler, T.; Rauk, A. *Inorg. Chem.* **1979**, *18*, 1558−1565 and 1755−1759.

(22) Diefenbach, A.; Bickelhaupt, F.; Matthias, Frenking, G. *J. Am. Chem. Soc.* **2000**, *122*, in press.

(23) Parr, R. G.; Pearson, R. G. *J. Am. Chem. Soc.* **1983**, *105*, 7512−7516.

(24) Chermette, H. *J. Comput. Chem.***1999**, *20*, 129−154 and references therein.

(25) Bersuker, I. B.; Gorinchoi, N. N.; Polinger, V. Z. *Theor. Chim. Acta* **1984**, *66*, 161−172.

(26) Shannon, R. D. *Acta Crystallogr. A* **1976**, *32*, 751−767.

(27) Meot-Ner(Mautner), M.; Wayne Sieck, L. *J. Am. Chem. Soc*. **1991**, *113*, 4448−4460.

(28) (a) Nikol, H.; Vogler, A. *J. Am. Chem. Soc.* **1991**, *113*, 8988−8990. (b) Vogler, A.; Nikol, H. *Comm. Inorg. Chem.* **1993**, *14*, 245−261.

(29) Pearson, R. G. *Coord. Chem. Rev.* **1990**, *100*, 403−425.

(30) (a) Pearson, R. G. *J. Chem. Educ.* **1987**, *64*, 561−567. (b) Pearson, R. G. *Chemical Hardness*, Wiley-VCH: Weinheim-New York, 1997; p 40.

(31) Datta, D. *J. Phys. Chem.* **1992**, *96*, 2409−2410.

(32) Parr, R. G.; Chattaraj, P. K. *J. Am. Chem. Soc.* **1991**, *113*, 1854−1855.

(33) Sebastian, K. L. *Chem. Phys. Lett.* **1994**, *231*, 40−42.

(34) Wang, S. Y.; Lohr, L. L., Jr. *J. Chem. Phys.* **1974**, *60*, 3901−3915.

(35) Schmidtke, H.-H.; Degen, J. *Struct. Bonding* **1989**, *71*, 99−124.

(36) Polinger, V. Z.; Gorinchoi, N. N.; Bersuker, I. B. *Chem. Phys.* **1992**, *159*, 75−87.

(37) Durand, Ph.; Malrieu, J. P. In *Ab Initio Methods in Quantum Chemistry − I*; Lawley, K. P., Ed.; John Wiley & Sons Ltd. *Adv. Chem. Phys.* Wiley: New York, 1987; Vol. 67, pp 321−412 and references therein.

(38) des Cloizeaux, J. *Nucl. Phys.* **1960**, *20*, 321−346.